Elastic-viscoplastic self-consistent modeling for finite deformation of polycrystalline materials

Materials Science & Engineering A 799 (2021) 140325

Contents lists available at ScienceDirect

Materials Science & Engineering A

journal homepage: http://www.elsevier.com/locate/msea

Elastic-viscoplastic self-consistent modeling for finite deformation of polycrystalline materials

Hongjia Li [a,b,c,*], Fredrik Larsson [a], Magnus Hörnqvist Colliander [b], Magnus Ekh [a,**]

[a] Department of Industrial and Materials Science, Chalmers University of Technology, SE, 41296, Göteborg, Sweden
[b] Department of Physics, Chalmers University of Technology, SE, 41296, Göteborg, Sweden
[c] Key Laboratory of Neutron Physics and Institute of Nuclear Physics and Chemistry, China Academy of Engineering Physics, Mianyang, 621999, PR China

ARTICLE INFO

Keywords:
Elastic-viscoplastic self-consistent (EVPSC) model
In situ neutron Diffraction
Polycrystalline materials
Finite deformation

ABSTRACT

Anisotropic 1-site and 2-site self-consistent models are developed to describe the elastic-viscoplastic behavior of polycrystalline materials deformed to finite strains on the basis of rate-dependent crystallographic slip and a generalized Hill-Hutchinson self-consistent approach. The choice of rate-dependent constitutive law at single crystal level implemented in the models is discussed through fitting experimental data and calibrating viscous parameters. It is found that drag-stress type Norton law works well for the 1-site elastic-viscoplastic self-consistent (EVPSC) model while threshold stress type Norton law is suitable for the 2-site EVPSC model to assure that the viscoplastic inter-granular interaction is realistic. Both models have been verified by thoroughly fitting experimental data in literatures. For the 1-site EVPSC model, selected experimental data covers both macroscopic and microscopic mechanical responses of steels during deformation with a large range of strain rate from the quasi-static (10^{-4} s^{-1}) to the dynamic ($\sim 10^{4}$ s^{-1}). For the 2-site EVPSC model, *in situ* neutron diffraction data of nickel-based superalloys with various microstructures was fitted. Both models generally fit the experimental data well. A comparison between the EVPSC and elastic-plastic self-consistent (EPSC) models on the prediction of lattice strains has also been made for both the 1-site and 2-site cases, which verifies the predictability on lattice strains of the newly developed EVPSC models. A validation of the homogenization approach for the EVPSC modeling has been performed, which confirms that the proposed EVPSC models are applicable for cubic structure materials with finite deformations. Our formulation of EVPSC modeling developed in this work shines a spotlight on the way of developing a multi-functional self-consistent model to predict both macroscopic and microscopic deformation behaviors of various polycrystalline materials under different loading rates of 10^{-4} s^{-1} $\sim 10^{4}$ s^{-1}.

1. Introduction

In situ diffraction is a superior technique to provide fundamental understanding of microscopic deformation of various polycrystalline metals by quantifying the evolution of lattice strains within the bulk of the materials [1–9]. Since the individual reflections are contributed from subsets of grains due to the large penetration depth and large gauge volume, self-consistent (SC) modeling is often used to quantitatively interpret the experimental data by correlating the macroscopic behavior of heterogeneous materials with the knowledge of their single crystals [1–5,9–11].

Most widely used SC models are the elastic-plastic self-consistent (EPSC) model [12] and the viscoplastic self-consistent (VPSC) model [13] for single phase materials applications. These models are developed based on the Hill-Hutchinson approach [14,15]. The model assumptions are that all grains have an ellipsoidal shape and that they are embedded in an infinite homogeneous equivalent medium (HEM), which properties are the homogenized (weighted average) of all the grains. The Eshelby's solution [16] then gives a uniform stress and strain in each grain. The effect of grain morphology on stress and strain accommodation is considered in this inclusion formalism in comparison with the full constraint Taylor approach [17]. Since most of the structural materials are precipitation strengthened alloys in the rapid developing field of aerospace technology, recent efforts on the development of SC models have been motivated by the need of capturing the deformation behaviors of individual phases in such alloys. In these alloys, such as titanium (Ti)

* Corresponding author. Department of Industrial and Materials Science, Chalmers University of Technology, SE, 41296, Göteborg, Sweden.
** Corresponding author. Department of Industrial and Materials Science, Chalmers University of Technology, SE, 41296, Göteborg, Sweden
E-mail addresses: lihongjia_caep@126.com (H. Li), magnus.ekh@chalmers.se (M. Ekh).

https://doi.org/10.1016/j.msea.2020.140325
Received 31 July 2020; Received in revised form 21 September 2020; Accepted 25 September 2020
Available online 2 October 2020

alloys [18] and nickel-based (Ni-based) superalloys [19], the precipitation and parent phases have specific orientation relationship. Thus, 2-site SC models are required to account for the strong correlation in morphology and orientation between neighbor grains due to the vicinity effect between the two phases. Lebensohn and Canova pioneered the development of 2-site SC modeling by considering two interacting grains of different phases deforming in the HEM [20]. They developed a 2-site large strain VPSC model and applied it to two Ti alloys exhibiting different microstructures. Texture formation for various microstructures was well predicted and discussed. An important limitation is that VPSC models do not involve elastic strains and hence cannot be used to compare against lattice strains measured by *in situ* neutron diffraction. A 2-site EPSC model was formulated by Daymond *et al.* [10] where the ellipsoidal pair deforms as a unit in the HEM and that effective eigen-strain is uniform. In Ref. [1,4,10], this model was used to simulate the lattice strain evolution of Ni-based superalloys with different γ' microstructures at ambient and elevated temperatures. However, only strains up to 3% was studied and no lattice rotation or texture development was accounted for. Recently, Li *et al.* [11] have addressed the issue and implemented a 2-site EPSC model for finite strain applications. The model has been verified by well fitting various data sets of *in situ* lattice strains of Ni-based superalloys measured by neutron diffraction technique.

Although EPSC and VPSC models for both single phase and two-phase materials at finite deformation applications have been well developed, the EPSC models cannot simulate rate-dependent problems since it neglects the strain rate sensitivity of materials, while the VPSC models cannot simulate lattice strains since it neglects the elastic deformation. From this perspective, the elastic-viscoplastic self-consistent (EVPSC) model [21–26] is more appropriate to study the experimentally observed relaxation and creep associated with finite hold time for data acquisition of the *in situ* neutron diffraction, where both elasticity and strain rate relativity are considered. In the above mentioned models, the material properties (strain, stress, and strain rate) are assumed to be uniform within the ellipsoidal inclusion and in the infinite HEM. Indeed, the distribution of strain and stress within an inclusion is non-uniform for non-linear viscous materials, *i.e.* the matrix displays viscoplastic heterogeneity. Nevertheless, the assumption of the uniformities is an acceptable approximation of the Eshelby inclusion problem for non-linear viscous cases, which has been verified with a good agreement by comparing to the results calculated by finite element method for various inclusion shapes and loading conditions [27,28]. Moreover, Wang *et al.*'s 1-site EVPSC model [24,25] has been largely utilized in fitting *in situ* neutron experimental data of face-centered cubic (f.c.c.) structure 316 L austenitic stainless steels [29,30] and hexagonal close-packed (h.c.p.) structure magnesium [25,31,32] and zirconium [33] alloys. Good agreements between simulated results and experimental data are obtained. It should be emphasized that the EVPSC model can reproduce monotonic, stress relaxation, and strain creep results of stress-strain curves and lattice strain evolutions with a single set of hardening parameters, while the EPSC model needs three different sets of hardening parameters to fit the three cases separately due to the fact that the EPSC model does not account for the physical mechanisms of viscous behavior [29]. It thus can be seen that the EVPSC model is superior to the EPSC model in fitting *in situ* neutron diffraction data where stress relaxation or strain creep often occurs during data acquisition. However, to the authors' knowledge, there is no general anisotropic EVPSC modeling for both single phase and multi-phase materials applications.

The objective of the present paper is to develop anisotropic 1-site and 2-site EVPSC models applicable for finite deformation of single phase and two-phase polycrystalline materials on the basis of rate-dependent crystallographic slip and a generalized version of Hill-Hutchinson SC approach. At single crystal level, two types of Norton law are implemented to describe the rate-dependent constitutive relation, where stiffness tensor is used as that often utilized in EPSC models, in contrast with the most widely employed VPSC [13,20] and 1-site EVPSC models [24] where compliance tensor is used. Since the SC models with various deformation systems involve a large number of fitting parameters, it is difficult to determine them univocally. A convincing way to reduce the number of suitable parameter combinations is not only fitting the macroscopic stress-strain curves and deformed textures, but also simultaneously fitting the microscopic lattice strains measured by *in situ* neutron diffraction. The proposed EVPSC models are verified by doing so. In Section 2, the formulations and implementations of the 1-site and 2-site EVPSC models are given. Further, in Section 3 the results are given for single phase steels and two-phase Ni-based superalloys with a detailed discussion, and discussion on the validation of the homogenization approach for the EVPSC models developed in this work. Finally, in Section 4 we give some general conclusions.

2. Modeling

2.1. Constitutive relations for rate-sensitive single crystals

The elastic constitutive equation for a crystal is specified by Hooke's law:

$$\dot{\boldsymbol{\sigma}}_c = \mathbf{E} : \left(\dot{\varepsilon}_c - \dot{\varepsilon}_c^p\right) = \mathbf{E} : \left(\dot{\varepsilon}_c - \sum_\alpha \dot{\gamma}_c^\alpha m_c^\alpha\right) \tag{1}$$

where $\dot{\boldsymbol{\sigma}}_c$, $\dot{\varepsilon}_c$, $\dot{\varepsilon}_c^p$ are the stress rate, the strain rate, and the plastic strain rate, respectively. $\mathbf{E}$ is the elastic stiffness, $\dot{\gamma}_c^\alpha$ is the shear rate on the α-th slip system, and the symmetric Schmid tensor is defined in terms of the slip direction ($\boldsymbol{b}_c^\alpha$) and slip-plane normal ($\boldsymbol{n}_c^\alpha$) as $\boldsymbol{m}_c^\alpha = \mathrm{sym}(\boldsymbol{b}_c^\alpha \otimes \boldsymbol{n}_c^\alpha)$. In order to specify $\dot{\gamma}_c^\alpha$ to complete the constitutive function, Norton law is assumed for the definition of the viscoplastic multiplier:

$$\dot{\gamma}_c^\alpha\left(\boldsymbol{\sigma}_c,\ \tau_c^\alpha\right) = \frac{1}{t_*}\frac{\langle \Phi_c^\alpha(\boldsymbol{\sigma}_c,\ \tau_c^\alpha)\rangle^m}{C^m} = \dot{\gamma}_c^0\frac{\langle \Phi_c^\alpha(\boldsymbol{\sigma}_c,\ \tau_c^\alpha)\rangle^m}{C^m} \tag{2}$$

where t_* is the natural relaxation time, and we define $\dot{\gamma}_c^0 = 1/t_*$ as a shear rate parameter in this work. m is the rate-sensitive exponent, the inverse of which ($1/m$) is strain rate sensitivity. C is a constant set to be 1 MPa to deduct the unit. Here, $\langle \bullet \rangle$ is the McCauley bracket defined as:

$$\left\langle \Phi_c^\alpha\left(\boldsymbol{\sigma}_c, \tau_c^\alpha\right)\right\rangle = \begin{cases} \Phi_c^\alpha\left(\boldsymbol{\sigma}_c,\ \tau_c^\alpha\right) & \text{If} \quad \Phi_c^\alpha\left(\boldsymbol{\sigma}_c,\ \tau_c^\alpha\right) > 0 (3a) \\ 0 \quad \text{If} \quad \Phi_c^\alpha\left(\boldsymbol{\sigma}_c,\ \tau_c^\alpha\right) \le 0 (3b) \end{cases}$$

where $\Phi_c^\alpha(\boldsymbol{\sigma}_c,\ \tau_c^\alpha)$ is the yield function of slip system α mainly depending on the stress in the crystal and the resistance of the slip system. There are at least two ways to define it. The most commonly used one is to divide by τ_c^α, as shown in Eq. (4a) [13,15,21,22,24]. The other one is to subtract by τ_c^α and thereby interpret it as a threshold hardening stress (Eq. (4b)), as introduced in text books [34,35]. Both are employed in this work. With Eqs. (4a) and (4b), we define the Norton law as Type I and Type II, respectively.

$$\Phi_c^\alpha\left(\boldsymbol{\sigma}_c,\ \tau_c^\alpha\right) = \begin{cases} \left|\dfrac{\boldsymbol{\sigma}_c : \boldsymbol{m}_c^\alpha}{\tau_c^\alpha}\right| (4a) \\ \boldsymbol{\sigma}_c : \boldsymbol{m}_c^\alpha - \tau_c^\alpha (4b) \end{cases}$$

For the actual computations, the shear rate of the α-th slip system $\dot{\gamma}_c^\alpha$ must be estimated for each time increment. Here, we do linearization around ${}^n\boldsymbol{\sigma}_c$ and ${}^n\tau_c^\alpha$ from previous time step t_n:

$$\dot{\gamma}_c^\alpha\left(\boldsymbol{\sigma}_c,\ \tau_c^\alpha\right) \approx \dot{\gamma}_c^\alpha\left({}^n\boldsymbol{\sigma}_c,\ {}^n\tau_c^\alpha\right) + \left.\frac{\partial\dot{\gamma}_c^\alpha}{\partial\boldsymbol{\sigma}_c}\right|_{t=t_n} : \left(\boldsymbol{\sigma}_c - {}^n\boldsymbol{\sigma}_c\right) + \left.\frac{\partial\dot{\gamma}_c^\alpha}{\partial\tau_c^\alpha}\right|_{t=t_n}\left(\tau_c^\alpha - {}^n\tau_c^\alpha\right) \tag{5}$$

with

$$\frac{\partial \dot{\gamma}_c^\alpha}{\partial \boldsymbol{\sigma}_c} = m\dot{\gamma}_c^0 \frac{\boldsymbol{m}_c^\alpha}{\tau_c^\alpha} \frac{\langle \Phi_c^\alpha(\boldsymbol{\sigma}_c,\ \tau_c^\alpha)\rangle^{m-1}}{C^m} \frac{\boldsymbol{\sigma}_c : \boldsymbol{m}_c^\alpha}{|\boldsymbol{\sigma}_c : \boldsymbol{m}_c^\alpha|} \quad \text{or} \quad m\dot{\gamma}_c^0 \boldsymbol{m}_c^\alpha \frac{\langle \Phi_c^\alpha(\boldsymbol{\sigma}_c,\ \tau_c^\alpha)\rangle^{m-1}}{C^m} \tag{6a}$$

$$\frac{\partial \dot{\gamma}_c^\alpha}{\partial \tau_c^\alpha} = -m\dot{\gamma}_c^0 \frac{\langle \Phi_c^\alpha(\boldsymbol{\sigma}_c,\ \tau_c^\alpha)\rangle^{m-1}}{C^m} \frac{|\boldsymbol{\sigma}_c : \boldsymbol{m}_c^\alpha|}{(\tau_c^\alpha)^2} \quad \text{or} \quad -m\dot{\gamma}_c^0 \frac{\langle \Phi_c^\alpha(\boldsymbol{\sigma}_c,\ \tau_c^\alpha)\rangle^{m-1}}{C^m} \tag{6b}$$

$$\tau_c^\alpha - {}^n\tau_c^\alpha = \dot{\tau}_c^\alpha\, \Delta t = \frac{d\tau_c^\alpha}{d\gamma_c^{\mathrm{acc}}} \sum_\beta h_{\alpha\beta}\, \dot{\gamma}_c^\beta\, \Delta t \tag{6c}$$

In Eqs. (6a) and (6b), the first expression is for Type I (the drag-stress type) Norton law as shown in Eqs. (2) and (4a), and the second expression is for Type II (the threshold stress type) Norton law as shown in Eqs. (2) and (4b). In Eq. (6c), γ_c^{acc} is the accumulated shear strain in the crystal; $h_{\alpha\beta}$ are the latent hardening coupling coefficients, which are used to empirically account for the obstacles on system α from system β. τ_c^α is the critical resolved shear stress (CRSS) defined by an extended Voce hardening law [36]:

$$\tau_c^\alpha = \tau_0^\alpha + \left(\tau_1^\alpha + \theta_1^\alpha\, \gamma_c^{\mathrm{acc}}\right)\left(1 - \exp\left(-\frac{\theta_0^\alpha\, \gamma_c^{\mathrm{acc}}}{\tau_1^\alpha}\right)\right) \tag{7}$$

where τ_0^α, θ_0^α, θ_1^α, and $\tau_0^\alpha + \tau_1^\alpha$ are the initial CRSS, the initial hardening rate, the asymptotic hardening rate, and the back-extrapolated CRSS, respectively. It should be emphasized that all slip systems are active as soon as the resolved shear stress is different from zero for the case with Type I Norton law utilized, whereas only slip systems of which the resolved shear stress reaches the CRSS can be activated for the case with Type II Norton law employed.

Substituting Eq. (6c) into Eq. (5) with some manipulations, we can obtain:

$$\dot{\gamma}_c^\alpha\left(\boldsymbol{\sigma}_c,\ \tau_c^\alpha\right) = \sum_\beta \tilde{H}_{\alpha\beta}^{-1}\left(\dot{\gamma}_c^\beta\left({}^n\boldsymbol{\sigma}_c,\ {}^n\tau_c^\beta\right) + \left.\frac{\partial \dot{\gamma}_c^\beta}{\partial \boldsymbol{\sigma}_c}\right|_{t=t_n} : \left(\boldsymbol{\sigma}_c - {}^n\boldsymbol{\sigma}_c\right)\right) \tag{8}$$

where $\tilde{H}_{\alpha\beta}$ is the matrix notation of $\tilde{h}_{\alpha\beta}$, which has the following expression:

$$\tilde{h}_{\alpha\beta} = \delta_{\alpha\beta} - \left.\frac{\partial \dot{\gamma}_c^\alpha}{\partial \tau_c^\alpha}\right|_{t=t_n} \frac{d\tau_c^\alpha}{d\gamma_c^{\mathrm{acc}}}\, h_{\alpha\beta}\, \Delta t \tag{9}$$

where $\delta_{\alpha\beta}$is the Kronecker delta.

Inserting Eq. (8) into Eq. (1), the constitutive equation can be obtained with some manipulations:

$$\dot{\boldsymbol{\sigma}}_c = \mathbf{L}_c : \dot{\varepsilon}_c + \dot{\boldsymbol{\sigma}}_c^0 \tag{10}$$

with

$$\mathbf{L}_c = \mathbf{B}^{-1} : \mathbf{E} \tag{11a}$$

$$\dot{\boldsymbol{\sigma}}_c^0 = -\mathbf{B}^{-1} : \mathbf{E} : \sum_\alpha \sum_\beta \tilde{H}_{\alpha\beta}^{-1} \dot{\gamma}_c^\beta\, ({}^n\boldsymbol{\sigma}_c\ ,\ {}^n\tau_c^\beta) m_c^\alpha \tag{11b}$$

$$\mathbf{B} = \mathbf{I} + \mathbf{E} : \Delta t \sum_\alpha \sum_\beta \tilde{H}_{\alpha\beta}^{-1}\, \boldsymbol{m}_c^\alpha \otimes \left.\frac{\partial \dot{\gamma}_c^\beta}{\partial \boldsymbol{\sigma}_c}\right|_{t=t_n} \tag{11c}$$

2.2. Homogenization approach for EVPSC modeling

According to the SC approach developed by Hill and Hutchinson [14, 15], we assume an ellipsoidal elastic-viscoplastic single crystal (1-site) or two interacting ellipsoidal elastic-viscoplastic crystals of different phases (2-site) Ω_c embedded in an extended infinite homogeneous equivalent medium (HEM) $\Re^3$. The proposed homogenization approach aims at determining the macroscopic response of the extended infinite HEM with some specific boundary conditions, which is given by the relation between the macroscopic stress rate and strain rate tensors ($\dot{\bar{\boldsymbol{\sigma}}}$ and $\dot{\bar{\varepsilon}}$). The constitutive relation is assumed with the same format as Eq. (10). It thus has the following expressions within and outside of the crystal:

$$\dot{\boldsymbol{\sigma}} = \begin{cases} \mathbf{L}_c : \dot{\varepsilon} + \dot{\boldsymbol{\sigma}}_c^0 \text{in } \Omega_c (12a) \\ \overline{\mathbf{L}} : \dot{\varepsilon} + \dot{\bar{\boldsymbol{\sigma}}}_0 \text{in } \Re^3 \backslash \Omega_c (12b) \end{cases}$$

where $\overline{\mathbf{L}}$and $\dot{\bar{\boldsymbol{\sigma}}}_0$are the overall stiffness and relaxation stress rate tensors, respectively. In the absence of volume forces, the static equilibrium condition with a prescribed boundary condition imposes:

$$\begin{cases} -\dot{\boldsymbol{\sigma}} \cdot \nabla = 0 \text{in } \Re^3 (13a) \\ \boldsymbol{u} \to \bar{\varepsilon} \cdot \boldsymbol{x} \quad \text{as} \quad |\boldsymbol{x}| \to \infty \text{in } \Omega_c (13b) \end{cases}$$

Define $\dot{\boldsymbol{\tau}} = \dot{\boldsymbol{\sigma}} - \dot{\bar{\boldsymbol{\sigma}}} = \dot{\boldsymbol{\sigma}} - \overline{\mathbf{L}} : \dot{\varepsilon} - \dot{\bar{\boldsymbol{\sigma}}}_0$, then Eq. (13a) becomes (using $-\dot{\bar{\boldsymbol{\sigma}}} \cdot \nabla = 0$):

$$-\dot{\boldsymbol{\tau}} \cdot \nabla = 0 \quad \text{in} \quad \Re^3 \tag{14}$$

where

$$\dot{\boldsymbol{\tau}} = \begin{cases} \mathbf{L}_c : \dot{\varepsilon} - \overline{\mathbf{L}} : \dot{\bar{\varepsilon}} + \dot{\boldsymbol{\sigma}}_c^0 - \dot{\bar{\boldsymbol{\sigma}}}_0 \text{in } \Omega_c \left(15a\right) \overline{\mathbf{L}} : (\dot{\varepsilon} - \dot{\bar{\varepsilon}}) \text{in } \Re^3 \backslash \Omega_c & \left(15b\right) \end{cases}$$

According to Eshelby's equality, the stress and strain rates of the ellipsoidal inclusions in a HEM are equal for:

$$\dot{\boldsymbol{\sigma}}_c = \mathbf{L}_c : \dot{\varepsilon}_c + \dot{\boldsymbol{\sigma}}_c^0 = \overline{\mathbf{L}} : \left(\dot{\varepsilon}_c - \dot{\varepsilon}_c^*\right) + \dot{\bar{\boldsymbol{\sigma}}}_0 \tag{16}$$

where $\dot{\varepsilon} = \dot{\varepsilon}_c$ within the crystal, which is constant inside Ω_c. Here, $\dot{\varepsilon}_c^*$ is the eigenstrain rate satisfying:

$$-\overline{\mathbf{L}} : \dot{\varepsilon}_c^* = \left(\mathbf{L}_c - \overline{\mathbf{L}}\right) : \dot{\varepsilon}_c + \left(\dot{\boldsymbol{\sigma}}_c^0 - \dot{\bar{\boldsymbol{\sigma}}}_0\right) \tag{17}$$

We now define the strain rate deviation to be $\dot{\tilde{\varepsilon}} = \dot{\varepsilon} - \dot{\bar{\varepsilon}}$, then Eq. (15) can be rewritten as:

$$\dot{\boldsymbol{\tau}} = \begin{cases} \overline{\mathbf{L}} : \left(\dot{\tilde{\varepsilon}} - \dot{\varepsilon}_c^*\right) \quad \text{in } \Omega_c \quad \left(18a\right) \\ \overline{\mathbf{L}} : \dot{\tilde{\varepsilon}} \quad \text{in } \Re^3 \backslash \Omega_c \left(18b\right) \end{cases}$$

2.2.1. 1-Site EVPSC modeling

Eshelby introduced the Eshelby tensor **P**[16] that relates the eigenstrain rate $\dot{\varepsilon}_c^*$ and the strain rate deviation $\dot{\tilde{\varepsilon}}$ as [37]:

$$\dot{\tilde{\varepsilon}} = \mathbf{P} : \dot{\varepsilon}_c^* \tag{19}$$

Combining Eqs. (17) and (19) with some manipulations, we can obtain:

$$\dot{\varepsilon}_c = \mathbf{A}_c : \dot{\bar{\varepsilon}} - \mathbf{A}_c : \mathbf{P} : \overline{\mathbf{L}}^{-1} : \left(\dot{\boldsymbol{\sigma}}_c^0 - \dot{\bar{\boldsymbol{\sigma}}}_0\right) \tag{20}$$

where

$$\mathbf{A}_c = \left(\mathbf{I} + \mathbf{P} : \left(\overline{\mathbf{L}}^{-1} : \mathbf{L}_c - \mathbf{I}\right)\right)^{-1} \tag{21}$$

Inserting Eq. (20) into Eq. (12a) and taking weighted average on both sides of the equation, the following expression can be obtained:

$$\langle \dot{\boldsymbol{\sigma}}_c \rangle = \langle \mathbf{L}_c : \mathbf{A}_c \rangle : \dot{\bar{\varepsilon}} + \left\langle \dot{\boldsymbol{\sigma}}_c^0 - \mathbf{L}_c : \mathbf{A}_c : \mathbf{P} : \overline{\mathbf{L}}^{-1} : \left(\dot{\boldsymbol{\sigma}}_c^0 - \dot{\bar{\boldsymbol{\sigma}}}_0\right) \right\rangle \tag{22}$$

Comparing it with the macroscopic constitutive law (Eq. (12b)), we can identify:

$$\dot{\bar{\boldsymbol{\sigma}}} = \langle \dot{\boldsymbol{\sigma}}_c \rangle \tag{23a}$$

$$\overline{\mathbf{L}} = \langle \mathbf{L}_c : \mathbf{A}_c \rangle \tag{23b}$$

$$\dot{\bar{\boldsymbol{\sigma}}}_0 = \left\langle \dot{\boldsymbol{\sigma}}_c^0 - \mathbf{L}_c : \mathbf{A}_c : \mathbf{P} : \overline{\mathbf{L}}^{-1} : \left(\dot{\boldsymbol{\sigma}}_c^0 - \dot{\bar{\boldsymbol{\sigma}}}_0 \right) \right\rangle \tag{23c}$$

Then $\dot{\bar{\boldsymbol{\sigma}}}_0$can be solved from Eq. (23c) as:

$$\dot{\bar{\boldsymbol{\sigma}}}_0 = \left(\mathbf{I} - < \mathbf{L}_c : \mathbf{A}_c : \mathbf{P} > : \overline{\mathbf{L}}^{-1} \right)^{-1} : < \left(\mathbf{I} - \mathbf{L}_c : \mathbf{A}_c : \mathbf{P} : \overline{\mathbf{L}}^{-1} \right) : \dot{\boldsymbol{\sigma}}_c^0 > \tag{24}$$

2.2.2. 2-Site EVPSC modeling

For the 2-site case, there are two interacting ellipsoidal inclusions (#1 and #2) embedded in the extended infinite HEM. The eigenstrain rates $\dot{\varepsilon}_c^*$ and the strain rate deviations $\dot{\tilde{\varepsilon}}_c = \dot{\varepsilon}_c - \dot{\bar{\varepsilon}}$ are obtained by the four symmetric Eshelby tensors as [11,16,20]:

$$\dot{\tilde{\varepsilon}}_1 = \dot{\varepsilon}_1 - \dot{\bar{\varepsilon}} = \mathbf{P}_{11} : \dot{\varepsilon}_1^* + \mathbf{P}_{12} : \dot{\varepsilon}_2^* \tag{25a}$$

$$\dot{\tilde{\varepsilon}}_2 = \dot{\varepsilon}_2 - \dot{\bar{\varepsilon}} = \mathbf{P}_{21} : \dot{\varepsilon}_1^* + \mathbf{P}_{22} : \dot{\varepsilon}_2^* \tag{25b}$$

where $\mathbf{P}_{11}$ and $\mathbf{P}_{22}$ are the ordinary Eshelby tensors for the two inclusions; and $\mathbf{P}_{12}$ and $\mathbf{P}_{21}$ are the Eshelby tensors that connects the eigenstrain rate of one inclusion and the local deviation in strain rate of the other. For details regarding derivations and results for the 2-site Eshelby tensors we refer to Ref. [20,38].

In this subsection, we define the following notation for the subscript designations of the tensors for inclusions #1 and #2:

$$c = 1,\ 2 \quad \text{and} \quad \overline{c} = \begin{cases} 1 & c = 2 \quad (26a) \\ 2 & c = 1 \quad (26b) \end{cases}$$

Combining Eqs. (17) and (25) to eliminate the eigenstrain rates $\dot{\varepsilon}_c^*$, the following can be obtained with some manipulations:

$$\dot{\varepsilon}_c = \mathbf{A}_c : \dot{\bar{\varepsilon}} - \dot{\mathbf{H}}_c \tag{27}$$

where the concentration tensor $\mathbf{A}_c$ takes the form:

$$\mathbf{A}_c = \left(\mathbf{B}_{\overline{c}} : \mathbf{C}_c^{-1} : \mathbf{B}_c - \mathbf{C}_{\overline{c}} \right)^{-1} : \left(\mathbf{B}_{\overline{c}} : \mathbf{C}_c^{-1} + \mathbf{I} \right) \tag{28}$$

and the extra term $\dot{\mathbf{H}}_c$is:

$$\dot{\mathbf{H}}_c = \left(\mathbf{B}_{\overline{c}} : \mathbf{C}_c^{-1} : \mathbf{B}_c - \mathbf{C}_{\overline{c}} \right)^{-1} : \left(\dot{\mathbf{D}}_{\overline{c}} + \mathbf{B}_{\overline{c}} : \mathbf{C}_c^{-1} : \dot{\mathbf{D}}_c \right) \tag{29}$$

with

$$\mathbf{A}_d^* = \mathbf{I} - \overline{\mathbf{L}}^{-1} : \mathbf{L}_d \quad (d = c,\ \overline{c}) \tag{30a}$$

$$\mathbf{B}_c = \mathbf{I} - \mathbf{P}_{cc} : \mathbf{A}_c^* \tag{30b}$$

$$\mathbf{C}_c = \mathbf{P}_{c\overline{c}} : \mathbf{A}_{\overline{c}}^* \tag{30c}$$

$$\dot{\mathbf{D}}_c = \mathbf{P}_{cc} : \overline{\mathbf{L}}^{-1} : \left(\dot{\boldsymbol{\sigma}}_c^0 - \dot{\bar{\boldsymbol{\sigma}}}_0 \right) + \mathbf{P}_{c\overline{c}} : \overline{\mathbf{L}}^{-1} : \left(\dot{\boldsymbol{\sigma}}_{\overline{c}}^0 - \dot{\bar{\boldsymbol{\sigma}}}_0 \right) \tag{30d}$$

Inserting Eq. (27) into Eq. (12a) and taking weighted average on both sides of the equation, we can obtain the following equation:

$$\langle \dot{\boldsymbol{\sigma}}_c \rangle = \langle \mathbf{L}_c : \mathbf{A}_c \rangle : \dot{\bar{\varepsilon}} + \langle \dot{\boldsymbol{\sigma}}_c^0 - \mathbf{L}_c : \dot{\mathbf{H}}_c \rangle \tag{31}$$

Comparing it with the macroscopic constitutive law (Eq. (12b)), we can identify:

$$\dot{\bar{\boldsymbol{\sigma}}} = \langle \dot{\boldsymbol{\sigma}}_c \rangle \tag{32a}$$

$$\overline{\mathbf{L}} = \langle \mathbf{L}_c : \mathbf{A}_c \rangle \tag{32b}$$

$$\dot{\bar{\boldsymbol{\sigma}}}_0 = \langle \dot{\boldsymbol{\sigma}}_c^0 - \mathbf{L}_c : \dot{\mathbf{H}}_c \rangle \tag{32c}$$

Then $\dot{\bar{\boldsymbol{\sigma}}}_0$can be solved from Eq. (32c) as:

$$\dot{\bar{\boldsymbol{\sigma}}}_0 = \left(\mathbf{I} - \langle \mathbf{X}_{cc} + \mathbf{X}_{c\overline{c}} \rangle \right)^{-1} : \left\langle \left(\mathbf{I} - \mathbf{X}_{cc} \right) : \dot{\boldsymbol{\sigma}}_c^0 - \mathbf{X}_{c\overline{c}} : \dot{\boldsymbol{\sigma}}_{\overline{c}}^0 \right\rangle \tag{33}$$

where

$$\mathbf{X}_{cd} = \mathbf{L}_c : \left(\mathbf{B}_{\overline{c}} : \mathbf{C}_c^{-1} : \mathbf{B}_c - \mathbf{C}_{\overline{c}} \right)^{-1} : \left(\mathbf{B}_{\overline{c}} : \mathbf{C}_c^{-1} : \mathbf{P}_{cd} : \overline{\mathbf{L}}^{-1} + \mathbf{P}_{\overline{c}d} : \overline{\mathbf{L}}^{-1} \right) \quad (d = c\ ,\ \overline{c}) \tag{34}$$

2.3. Finite strain approach for EVPSC modeling

Texture evolution, finite strain formulation, and the update of material state should be incorporated in the EVPSC model for finite strain applications. The schemes are the same as that were employed for the EPSC models in Ref. [11,39]. Here, we summarize some mostly related ideas, and explain the implementation specifically for the 1-site and 2-site EVPSC models.

In order to account for texture evolution at arbitrary strains, the applied macroscopic rotation rate, local rotation rate, and crystal lattice rotation rate are calculated for rotations of the sample, ellipsoid, and crystal lattice, respectively. For the 2-site EVPSC model, crystal lattice co-rotation rate is used for each pair instead of using the individual ones. Due to the crystal lattice rotation (for the 1-site EVPSC model) or co-rotation (for the 2-site EVPSC model), all Cauchy stress rates are updated to the reference coordinate system by introducing the Jaumann rate of the Cauchy stress $\widehat{\boldsymbol{\sigma}}_c$ after solving the ellipsoidal inclusion equilibrium equation and reaching convergence. After reaching self-consistency, the shape and morphological orientation of each ellipsoid is updated, where the relative position of the two ellipsoids within each pair is also updated for the 2-site case. Detailed information and related equations are omitted here to avoid redundancy, which are provided in Appendix A.

3. Results and discussion

In this section, the applicability of the 1-site and 2-site EVPSC models to various rate-dependent deformations is checked by fitting the experimental data from published work [1,4,10,29,40,41]. Viscous parameters $\dot{\gamma}_c^0$ and m in Eq. (2) are identified for different cases and the validity of the homogenization approach is checked for the proposed EVPSC models in this work. It is noted that Type I Norton law (Eq. (2) and (4a)) is utilized for the 1-site EVPSC model and Type II Norton law (Eq. (2) and (4b)) is employed for the 2-site EVPSC model to fit the experimental data. The numerical code of the 1-site EVPSC model employed in this work is an update of the 1-site EPSC code (Version 4) developed by Tomé and coworkers written in Fortran 77 [12,39], and that of the 2-site EVPSC model is an update of the 2-site EPSC code developed by Li *et al.* [11]. Detailed results and discussion are given in the following subsections.

3.1. Application of 1-site EVPSC model to dynamic mechanical responses of steels at various strain rates and temperatures

The materials studied in this section are a 316 L stainless steel with f.c.c. structure [40] and a Fe-based high temperature alloy with body-centered cubic (b.c.c.) structure [41]. Both are single phase materials. The 1-site EVPSC model is used to simulate the stress-strain curves for the 316 L stainless steel deformed at strain rates of 1000 s^{-1}, 3000 s^{-1}, 5000 $s^{-1}$and temperatures of 20 °°C, 200 °°C, 400 °C, 800 °C, and that for the Fe-based high temperature alloy deformed at strain rates of 4f000 s^{-1}, 6000 s^{-1}, 9000 s^{-1}, 12000 s^{-1}at 20 °C and temperatures of 20 °C, 200 °C, 400 °C, 500 °C, 600 °C, 700 °C, 800 °C with a strain rate of 9000 s^{-1}. In the model, 500 grains with random initial texture are chosen for the two cases [29]. Activated slip system for the f.

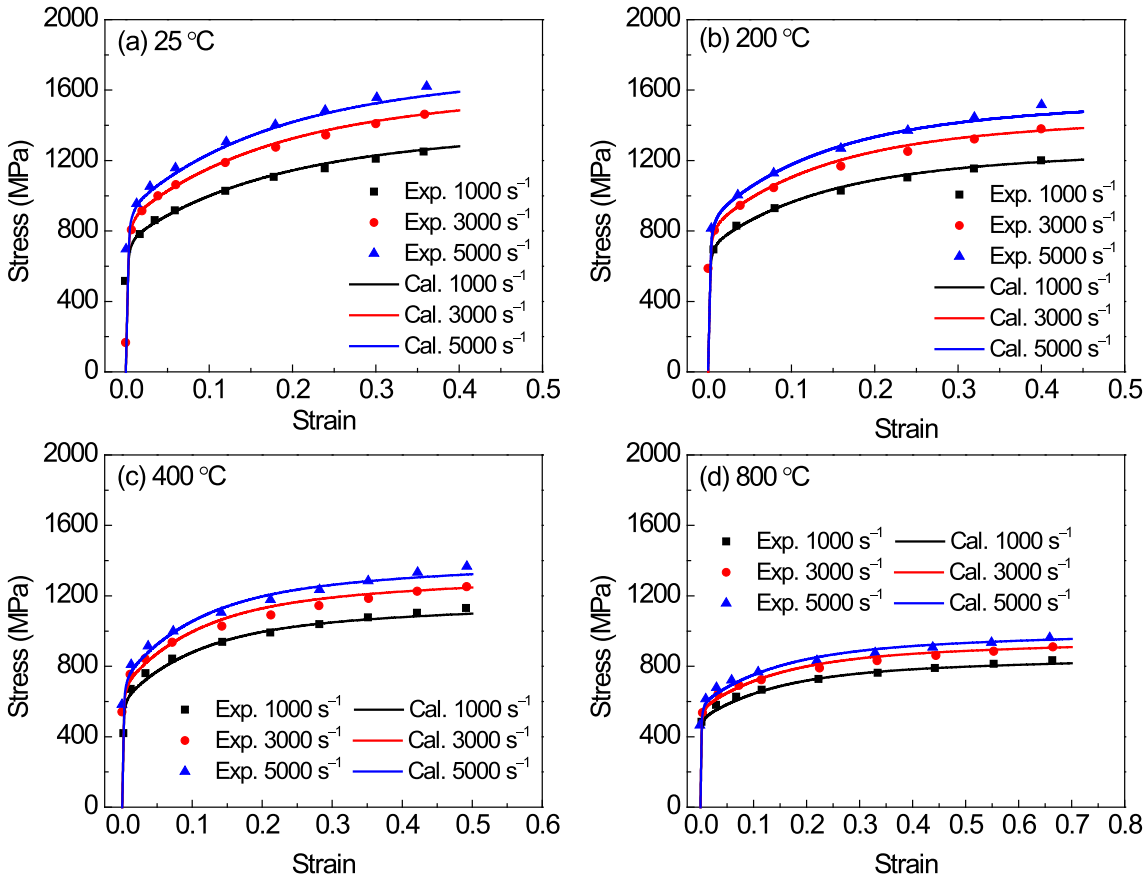

Fig. 1. Comparison of stress-strain curves measured (points, data from Ref. [40]) and simulated (lines) for a 316 L stainless steel deformed at different strain rates of 1000 s^{-1}, 3000 s^{-1}, 5000 s^{-1} and temperatures of (a) 25 °C, (b) 200 °C, (c) 400 °C, and (d) 800 °C.

c.c. 316 L stainless steel is {111}<110> and that for the b.c.c. Fe-based high temperature alloy is {110}<111> . Results are shown in Figs. 1 and 2, respectively. The predicted results generally fit the experimental data well.

The fitting parameters in the 1-site EVPSC model are the viscous parameters of $\dot{\gamma}_c^0$ and m as far as the flow rule (Eq. (2)) is concerned and coefficients of τ_0, τ_1, θ_0, θ_1 for the extended Voce hardening law (Eq. (7)). The shear rate $\dot{\gamma}_c^0$ is chosen constant to be 10^{-3} s^{-1} in this subsection since it has less effects on the simulated results than the rate-sensitive exponent m does. Other parameters used to best fit the experimental data are given in Table 1. The evolutions of m and $\tau_0$in terms of temperature for the two selected materials are plotted in Fig. 3 (a) and 3(b), respectively. It indicates that m increases (*i.e.* $1/m$increases) with increasing temperature at strain rates of 1000 s^{-1}, 3000 s^{-1}, 5000 s^{-1} for the 316 L stainless steel and the strain rate of 9000 s^{-1} for the Fe-based high temperature alloy. This is consistent with Larour et al. [42]. Since for a given strain rate with increasing temperature, more thermal energy fluctuation is available to overcome short range obstacles and the strain rate sensitivity of flow stress is then decreased. For the Fe-based high temperature alloy, a reasonable result is observed that τ_0 decreases with increasing temperature. However, for the 316 L stainless steel, τ_0 does not change much with increasing temperature. This may be because $\dot{\gamma}_c^0$ is also temperature dependent but chosen to be constant in this case. It is hard to accurately calibrate all the fitting parameters in the model with only knowing the macroscopic stress-strain curves. We hence do not discuss further about the parameters used for these dynamic compressions here. In order to know more details along with the macroscopic stress-strain curves, we calculated the stress relaxation curves at a strain of 0.01 with hold time $t_{hold} = 0.001$ s at different temperatures for the two alloys, as shown in Fig. 3(c) and (d), respectively. It reveals that the stress relaxes rapidly to a saturated value for all the studied cases and the amount of relaxation stress decreases with increasing temperature for both materials.

3.2. *Application of 1-site EVPSC model to static mechanical response of a 316 L austenitic stainless steel*

Wang et al. [29] have performed a comprehensive comparison among *in situ* neutron diffraction techniques used for measuring lattice strains: monotonic loading without interrupts, loading with strain holds (stress relaxation), and loading with stress holds (strain creep). A tangent compliance-based EVPSC modeling [24] is performed in the work to interpret the experimental data of a 316 L austenitic stainless steel. Both the experimental and numerical results reveal that the influence of the stress relaxation on the lattice strain evolution is more significant than that of the strain creep. A comparison between the EVPSC and EPSC models on the prediction of the three cases indicates that the EVPSC model is better suited to interpret *in situ* neutron diffraction data of rate-sensitive materials than the rate-insensitive EPSC model, especially when stress relaxation occurs during the traditional strain-controlled *in situ* neutron diffraction experiments. In this section, we will use the experimental data in Ref. [29] to verify our 1-site EVPSC model on the prediction of stress-strain curves and *in situ* lattice strains for the 316 L austenitic stainless steel with static loading modes of monotonic, relaxation, and creep.

In our model, 500 grains with random initial texture are chosen [29], and {111}⟨110⟩ type slip system is set to be active. The applied loading rate is 10^{-4} s^{-1}. Before fitting the experimental data, the rate-sensitive exponent m is calibrated with the initial shear rate $\dot{\gamma}_c^0$ set constant to be 10^{-3} s^{-1}. m is adjusted from 50 to 200 at a strain of 0.01 and a stress

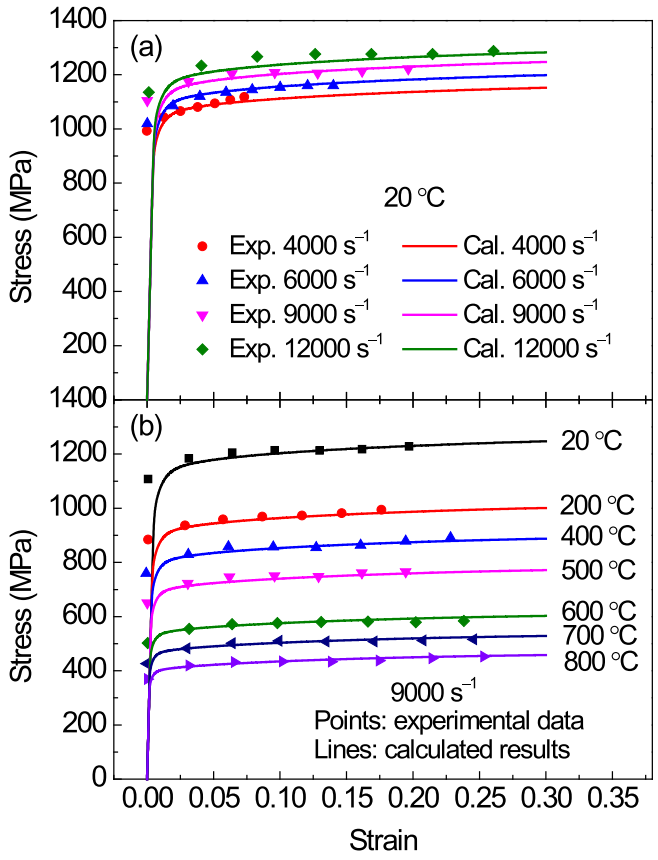

Fig. 2. Comparison of stress-strain curves measured (points, data from Ref. [41]) and simulated (lines) for a Fe-based high temperature alloy deformed at (a) different strain rates at 20 °C and (b) different temperatures with a strain rate of 9000 s^{-1}.

of 256 MPa with hold time t_{hold} = 900 s. Relaxation stress and creep strain for different m values are shown in Fig. 4. The respective stress and strain versus time curves for each case are shown in the embedded panels labeled as (a') and (b') in Fig. 4. The amount of relaxation stress and creep strain decreases with increasing m. The case $m = 66$ gives the most appropriate results in both relaxation stress and creep strain at the strain of 0.01 and the stress of 256 MPa for the alloy comparing to the experiments, which is later employed to fit the experimental data. Comparing to the strain rate sensitivity for the dynamic case of 316 L stainless steel ($1/m = 1/7.5 = 0.13$) discussed in Section 3.1, $1/m = 1/66 = 0.015$ is largely decreased for this quasi-static case. This is consistent with Larour et al. [42]. Since for a given temperature with decreasing the strain rate, more waiting time is necessary for dislocations to overcome short range obstacles, and therefore it is less strain rate sensitive. Coefficients describing the extended Voce hardening law (Eq. (7)) of $\tau_0 = 81.6$ MPa, $\tau_1 = 31.5$ MPa, $\theta_0 = 295$ MPa, $\theta_1 = 6.5$ MPa are determined to simultaneously predict the stress-strain curves and lattice strains measured with monotonic loading, relaxation, and creep. A comparison between the experimental data and the simulated results obtained with our 1-site EVPSC model is shown in Fig. 5. The calculated stress-strain curves for the three cases fit the experimental data well, as shown in Fig. 5(a–c). In order to fit the transverse lattice strains, data from 10 different directions perpendicular to the loading direction is collected and averaged since there are only 500 grains included in the model to speed up the simulation. Predicted lattice strains of {111}, {200}, and {220} reflections are shown in Fig. 5(g–i), where results labeled as "relaxation" and "creep" respectively are time-averaged values during 900 s hold. Comparing to the experimental data from Ref. [29], as re-plotted in Fig. 5(d–f), all the lattice strains are well predicted except the transverse lattice strains of {200} plane, which deviates from the experimental data during the elastic-plastic transition area. This is slightly better compared to the results predicted by the EPSC model in Ref. [29] if comparing Fig. 5(h) with Fig. 5(k). It should be noted that the rate-sensitive exponent m and the hardening parameters determined from our 1-site EVPSC model are not exactly the same as that used in Wang et al.'s EVPSC model [29], but they are quite similar, where $m = 66$ and $\tau_0 = 81.6$ MPa are set in this work while $m = 60$ and $\tau_0 = 84$ MPa are used in their work. It thus can be concluded that the proposed 1-site EVPSC model is applicable to the prediction of strain-rate-related relaxation and creep behaviors of cubic structure materials during *in situ* neutron diffraction experiments with similar viscous parameters and hardening coefficients as that used in Wang *et al.*'s EVPSC model [29].

3.3. Application of 2-site EVPSC model to axial lattice strains of Ni-based superalloys measured by neutron diffraction under static in situ tensile tests

Ni-based superalloys are composed of γ matrix and γ' precipitates with coherent interfaces [19], of which the *in situ* neutron diffraction data is suitable for checking a 2-site EVPSC model. In this section, we use the *in situ* neutron diffraction data of Alloy 720Li with a microstructure of two randomly intermixed size distribution of γ' precipitates at 20 °C, 400 °C, 500 °C, and 650 °C from Daymond et al. [10] to check our 2-site EVPSC model on the prediction of axial lattice strains.

In the model, 5000 grain pairs with random initial morphological and crystallographic orientation distributions are chosen, which is the same as that used in the 2-site EPSC model [11]. Spherical grains are assumed for both phases at the start of the simulation (see microscopy

Table 1
Parameters determined for the 1-site EVPSC model to best predict the experimental data of a 316 L stainless steel and a Fe-based high temperature alloy at various strain rates and temperatures. The hardening coefficients τ_0, τ_1, θ_0, and θ_1 are in MPa.

Exp. data	T (°C)	$\dot{\varepsilon}$(s^{-1})	Phase	m	Slip system	τ_0	τ_1	θ_0	θ_1
316 L stainless steel [40]	25	1000~5000	Austenite	7.5	{111}⟨110⟩	43	29	60	1.5
	200			8.0		46	28	70	1.3
	400			8.8		46	32	95	2.5
	800			10.5		48	25	58	1
Fe-based high temperature alloy [41]	20	4000	Low-carbon martensite	10.3	{110}⟨111⟩	86	6	17	0
		6000							
		9000							
		12000							
	200	9000	Low-carbon martensite	11.3	{110}⟨111⟩	78.5	6	17	0
	400			11.8		73.5	6	17	0
	500			12.5		68.5	6	17	0
	600			13.9		60.2	6	17	0
	700			14.5		55	6	17	0
	800			15.1		49.4	6	17	0

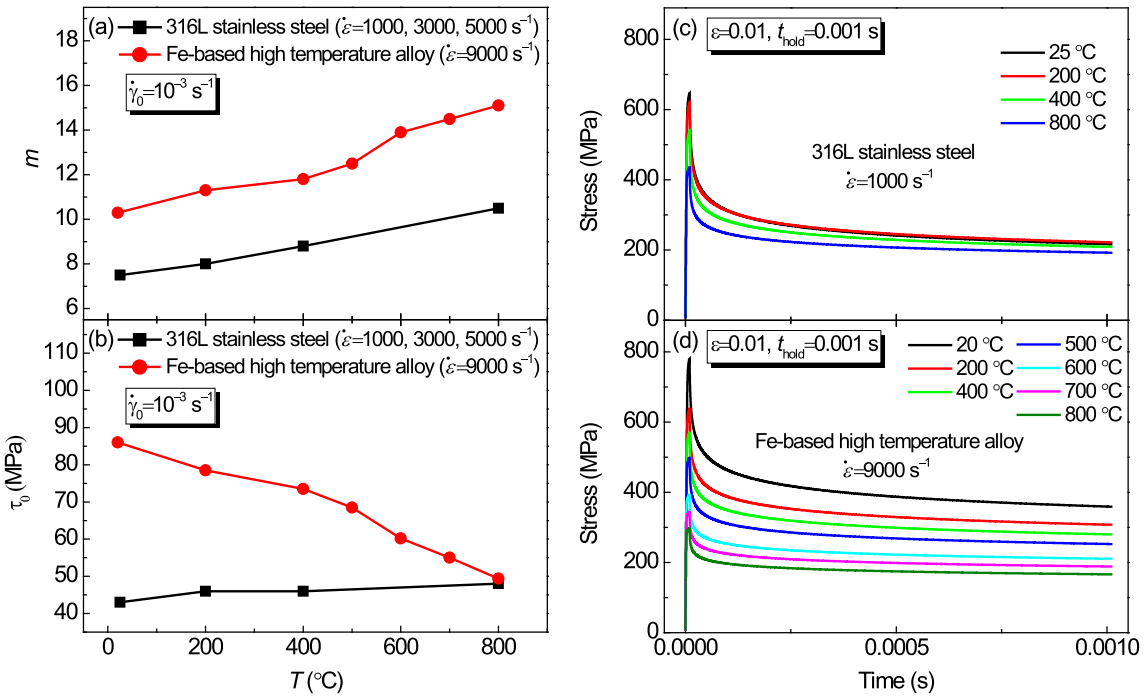

Fig. 3. Parameters used to best fit the experimental data measured at different strain rates for a 316 L stainless steel [40] and a Fe-based high-temperature alloy [41]: (a) the rate-sensitive exponent m and (b) the initial CRSS τ_0 as a function of temperature. The stress versus time curves for different cases at a strain of 0.01 with hold time t_{hold} = 0.001 sare shown in panels (c) and (d) for the 316 L stainless steel and the Fe-based high-temperature alloy, respectively.

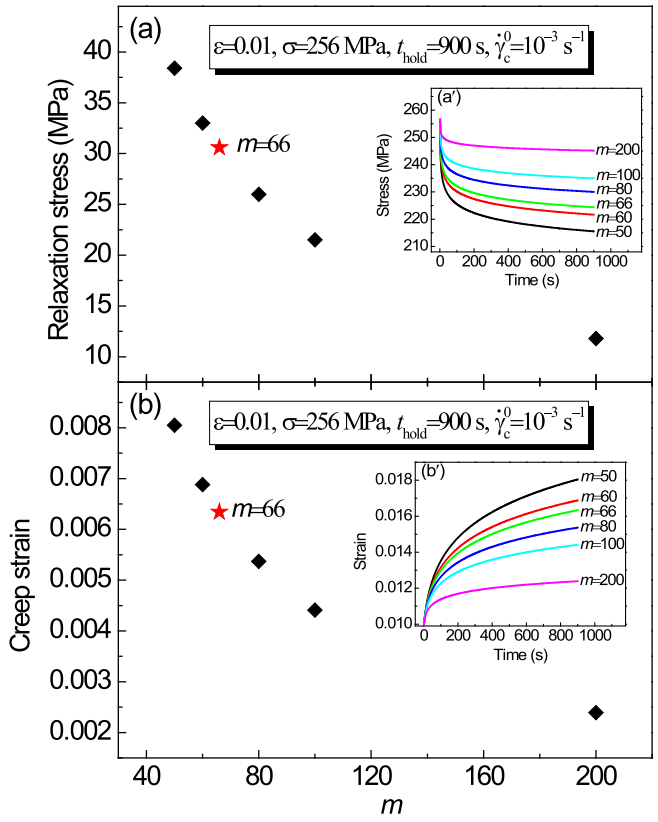

Fig. 4. Calibration of the rate-sensitive exponent m: (a) relaxation stress and (b) creep strain as a function of m at a strain of 0.01 and a stress of 256 MPa with hold time t_{hold} = 900 s. The corresponding stress and strain versus time curves are shown in the embedded panels named (a') and (b'), respectively.

pictures in Fig. 1 in Ref. [10]). The interaction factor $f_{\gamma-\gamma'}$ defining the interaction strength between γ and γ' grains [11] is set to be 1 for all the cases studied with the 2-site EVPSC model in this work to avoid extra uncertainties for the identification of the viscous parameters. All the cases are performed under uniaxial tension with a strain rate of $10^{-4}s^{-1}$, and monotonic loading mode is assumed in the model. In order to be consistent with the 1-site EVPSC model utilized to fit the experimental of single phase materials in Sections 3.1 and 3.2, Type I (drag-stress type, Eqs. (2) and (4a)) Norton law was first implemented in the 2-site EVPSC model. Calibrations of the viscous parameters of m within the range of 50 ~300 with fixed $\dot{\gamma}_c^0 = 10^{-3}$ $s^{-1}$and $\dot{\gamma}_c^0$ within the range of 10^{-10}~$1s^{-1}$ with fixed $m = 200$ were performed at a strain of 0.01 and a stress of 1148 MPa with hold time t_{hold} = 900 s. How the relaxation stress varies with respect to m and $\dot{\gamma}_c^0$ are shown in Fig. 6(a) and (b). It is found that the relaxation stress only depends on m at a specific strain and stress state in the case of employing Type I Norton law. Considering the computational error, a constant relaxation stress of about 40 ~41 MPa is observed with $m = 200$ as $\dot{\gamma}_c^0$ changes (Fig. 6(b)). According to the result shown in Fig. 6(a), a large rate-sensitive exponent $m = 200$ had to be used to give a reasonable relaxation stress of around 40 MPa for Ni-based superalloys at the strain of 0.01. Experimental data measured at 20 °C and 400 °C was fitted with $m = 200$ and $\dot{\gamma}_c^0 = 10^{-3}$ s^{-1}. Results are shown in Fig. 7(a and b) and 7(e-f), respectively. The amount of stress relaxation at various strains is shown on the macroscopic stress-strain curves as "drops", but not used for data process of lattice strains since monotonic loading mode is prescribed. Results predicted with the 2-site EPSC model [11] are also plotted in the figures as a comparison. Obvious deviations from the experimental data and the results predicted by the 2-site EPSC model during the elastic part and the elastic-plastic transition area can be observed for both temperatures (Fig. 7(b) and (f)). It may be because the grain-grain interaction between γ and γ' phases is not correctly captured with large m, according to the predicted results with the 2-site EPSC model for the cases that $f_{\gamma-\gamma'}$ is largely different from 1 (see Figs. 8 and 9 in Ref. [11]). Besides, Lebensohn and Tomé have estimated the viscoplastic behavior of

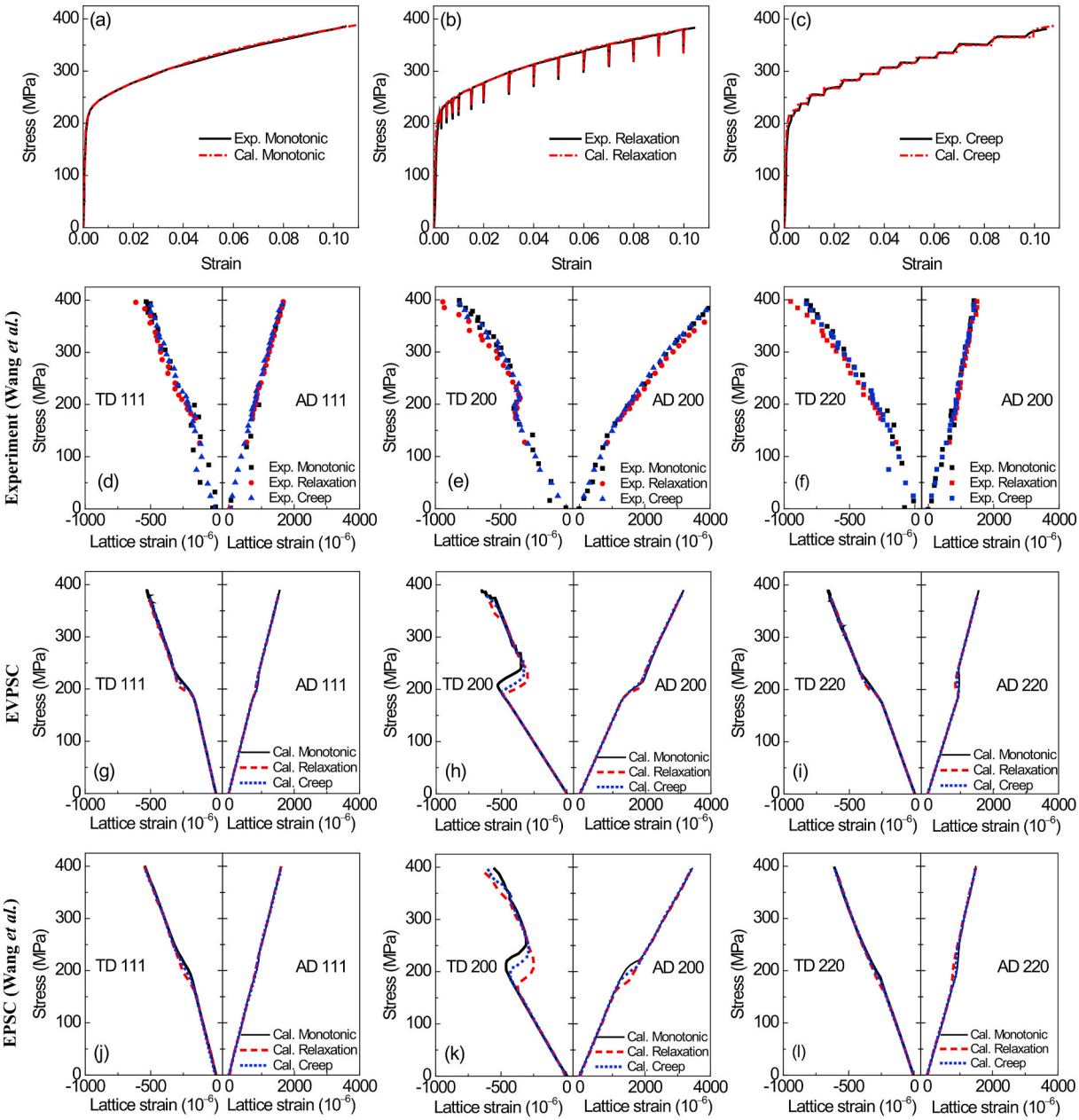

Fig. 5. Comparisons of measured and simulated stress-strain curves: (a) monotonic loading, (b) loading with strain holds (stress relaxation), and (c) loading with stress holds (strain creep), and lattice strains of {111}, {200}, and {220} planes: (d–f) measured by *in situ* neutron diffraction from Ref. [29], (g–i) simulated with the 1-site EVPSC model proposed in this work, and (j–l) simulated with EPSC model from Refs. [29]. AD and TD stand for axial direction and transverse direction, respectively.

anisotropic zirconium alloys and noticed that for values of m larger than 20, the VPSC model based on secant formulation loses its ability to describe realistic viscoplastic inter-granular interactions [13]. However, for Wang *et al.*'s 1-site EVPSC model [24] and our 1-site EVPSC model checked in Sections 3.1 and 3.2, which are both based on tangent formulation, respective $m = 60$ and $m = 66$ give good predictions on macroscopic stress-strain curves and microscopic lattice strains of the standard 316 L stainless steel simultaneously. These values of m are within the reasonable range of 50 ~66.7 for stainless steel, which is not rate-sensitive at room temperature [43]. Therefore, we decreased m to 60 and assumed high relaxation stresses of 117 MPa and 122 MPa, respectively, for the temperatures of 20 °C and 400 °C at the strain of 0.01 according to Fig. 6(a) to reach the relaxed state. Similar results of lattice strains to the cases with $m = 200$ were obtained, as shown in Fig. 7(d) and (h). It thus can be concluded that the 2-site EVPSC model with Type I Norton law implemented does not describe realistic viscoplastic grain-grain interactions.

In [22], a "threshold" shear stress $\tau_X$is suggested to be included in the description of shear rate $\dot{\gamma}_c^\alpha$ with drag-stress type Norton law (Type I, Eqs. (2) and (4a)) to remove the rate-sensitive character without using large rate-sensitive exponent m, *i.e.* $\Phi_c^\alpha = \frac{\sigma_c : m_c^\alpha - \tau_X}{\tau_c^\alpha}$, which is an extension of Eq. (4a). In our case, we use $\Phi_c^\alpha = \boldsymbol{\sigma}_c : \boldsymbol{m}_c^\alpha - \tau_c^\alpha$ instead, *i.e.* Type II (Eq. (2) and (4b)), in order to explicitly present a "threshold" shear stress as traditionally used in solid mechanics [34,35]. With Type II Norton law implemented in the 2-site EVPSC model, calibrations of the viscous parameters of m within the range of 3 ~8 with fixed $\dot{\gamma}_c^0 = 10^{-9}\ s^{-1}$ and $\dot{\gamma}_c^0$ within the range of 10^{-10}~$10^{-3} s^{-1}$ with fixed $m = 4$are also done at the strain of 0.01 and the stress of 1148 MPa with hold time $t_{hold} = 900$ s. Results are shown in Fig. 6(c and d), which demonstrate that the

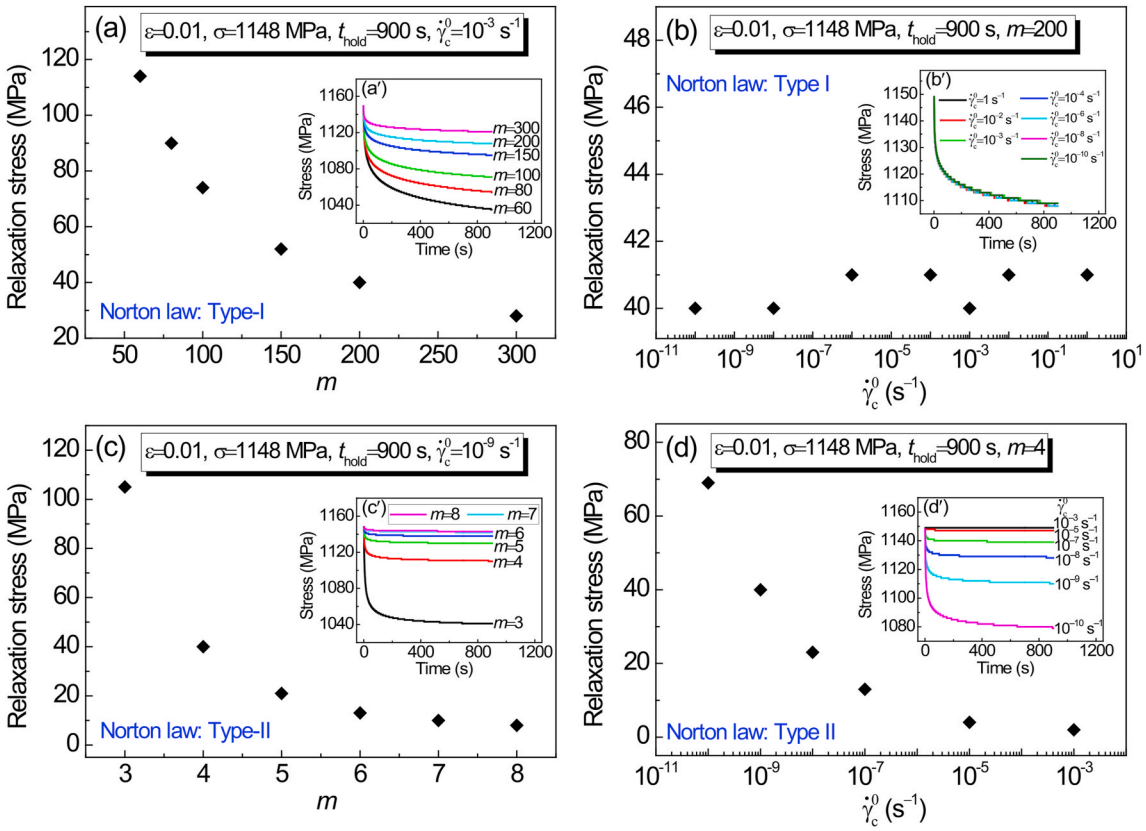

Fig. 6. Calibration of viscous parameters utilized in Type I Norton law: relaxation stress as a function of (a) m with fixed $\dot{\gamma}_c^0 = 10^{-3}s^{-1}$, (b) $\dot{\gamma}_c^0$ with fixed $m = 200$, and Type II Norton law: relaxation stress as a function of (c) m with fixed $\dot{\gamma}_c^0 = 10^{-9}s^{-1}$, and (d) $\dot{\gamma}_c^0$ with fixed $m = 4$ at a strain of 0.01 and a stress of 1148 MPa with hold time $t_{hold} = 900$ s. It is noted that m is the rate-sensitive exponent and $\dot{\gamma}_c^0$ is the shear rate parameter. The corresponding stress versus time curves are shown in the embedded figures named (a'–d'), respectively.

relaxation stress decreases with increasing m and $\dot{\gamma}_c^0$. The relaxation stresses of 40 MPa, 43 MPa, 35 MPa, 37 MPa are obtained at the strain of 0.01 at 20 °C, 400 °C, 500 °C, and 650 °C by assuming $m = 4$ and $\dot{\gamma}_c^0 = 10^{-9}$ s^{-1} in the model for Alloy 720Li studied in Ref. [10]. A comparison of measured and simulated stress-strain curves and lattice strains for the alloy is shown in Fig. 8. The predicted lattice strains with Type II Norton law implemented in the 2-site EVPSC model generally fit the experimental data well, which also approach the simulated results with the 2-site EPSC model [11] except for the 500 °case at relatively large strains where the total deformation is large ($\varepsilon = 0.3$). Nevertheless, the anomalous behavior of Ni-based superalloys [44] below the peak strength temperature around 500 °is captured by the 2-site EVPSC model.

A further comparison is made between the 2-site EVPSC model with Type II Norton law implemented and the 2-site EPSC model [11] on the prediction of evolution of the average number of active systems per grain (AVACS), relative activity of {111}⟨110⟩ and {100}⟨110⟩ slip systems in γ' phase, deformed texture, and phase specific stress of γ and γ' phases for Alloy 720Li at 20 °C, 400 °C, 500 °C, and 650 °C. Results are shown in Fig. 9 ~11. Fig. 9(a), (c), (e), and (g) indicate that slip systems are more easily activated in the 2-site EVPSC model in contrast to that in the 2-site EPSC model, where the slip systems are activated earlier and the AVACS is much larger. Both models give the same general conclusion that the AVACS of γ phase is larger than that of γ' at 20 °C, but it reverses at 400 °Cand 500 °C, and then reverses back at 650 °C. Evolutions of the relative activity of {111}⟨110⟩ and {100}⟨110⟩slip systems in γ'phase predicted with the two models at 20 °C, 400 °C, 500 °C, and 650 are shown in Fig. 9(b), (d), (f), and (h), respectively. At 20 ° , only {111}⟨110⟩ slip system is activated and it starts earlier in the 2-site EVPSC model than that in the 2-site EPSC model. At high temperatures, both {111}⟨110⟩ and {100}⟨110⟩ slip systems are activated with {100}⟨110⟩ starting earlier and {111}⟨110⟩starting later in the 2-site EVPSC model than that in the 2-site EPSC model. Big differences at 500 °C and 650 °C are observed. At 500 °C, the relative activity of {111}⟨110⟩ and {100}⟨110⟩ slip systems alternates twice as predicted with the 2-site EPSC model; however, the alternation predicted by the 2-site EVPSC model occurs later. At 650 °C, {100}⟨110⟩ slip system is predominant first and then {111}⟨110⟩ slip system becomes more active after a few plastic deformations predicted with the 2-site EVPSC model, which is different from the result obtained with the 2-site EPSC model where {100}⟨110⟩slip system is predominant during the whole deformation. These differences in the evolution of deformation mechanisms predicted with the two models have an accumulated effect on the simulated grain orientation distribution. Fig. 10 shows the deformed textures predicted with the two models. A comparison of the predicted fiber volume of ⟨111⟩, ⟨110⟩, and ⟨100⟩ components parallel to the tensile axis (*i.e.* AD) between the two models is presented for each temperature. Pole figures predicted with the 2-site EVPSC model are embedded in each panel, and that predicted with the 2-site EPSC model can be found in Fig. 6 in Ref. [11], which were obtained by using the MTEX open-source package [45]. A similar texture is displayed for the two models when the ⟨111⟩ fiber is strengthened and the ⟩ ⟨110⟩ fiber is weakened during plastic deformation. But for the 2-site EVPSC model the ⟨111⟩fiber becomes weaker and the ⟨110⟩fiber stronger as compared to that from the 2-site EPSC model (Fig. 10). The strength of the ⟨100⟩fiber predicted by the two models is almost the same. Nevertheless, results of the evolution of phase specific stress of γ and γ' phases calculated with the two models are quite close for the four temperatures, as shown in Fig. 11. Lastly, the reference hardening of individual slip systems in γ and γ'phases used in

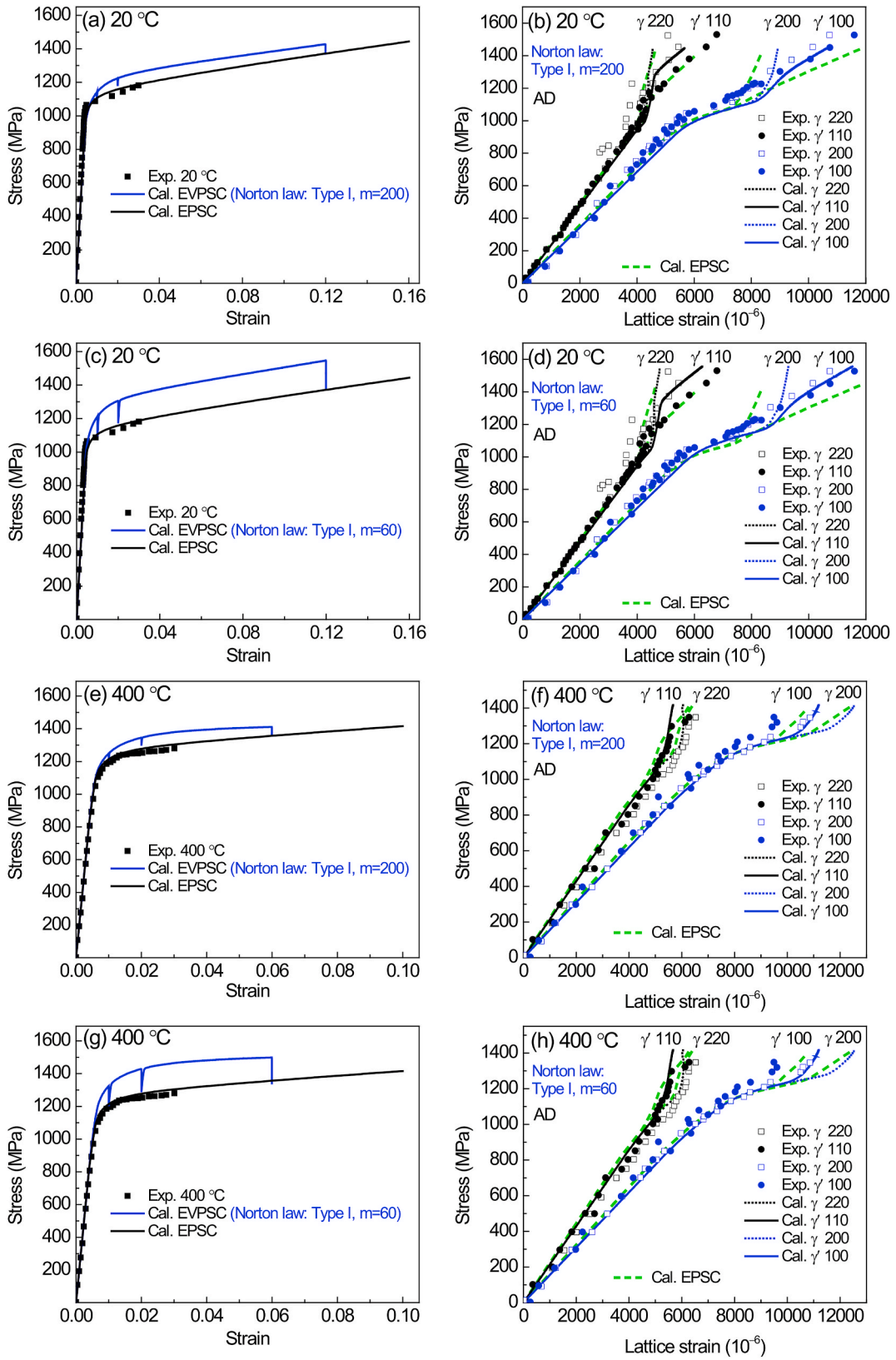

Fig. 7. Comparison of stress-strain curves and axial lattice strains measured (points, data from Ref. [10]) and simulated (lines) for Alloy 720Li utilizing Type I Norton law with fixed shear rate parameter $\dot{\gamma}_c^0 = 10^{-3}s^{-1}$: (a–b) 20 °C, $m = 200$, (c–d) 20 °C, $m = 60$, (e–f) 400 °C, $m = 200$, and (g–h) 400 °C, $m = 60$. Results predicted with the 2-site EPSC model are shown as a comparison. AD stands for axial direction.

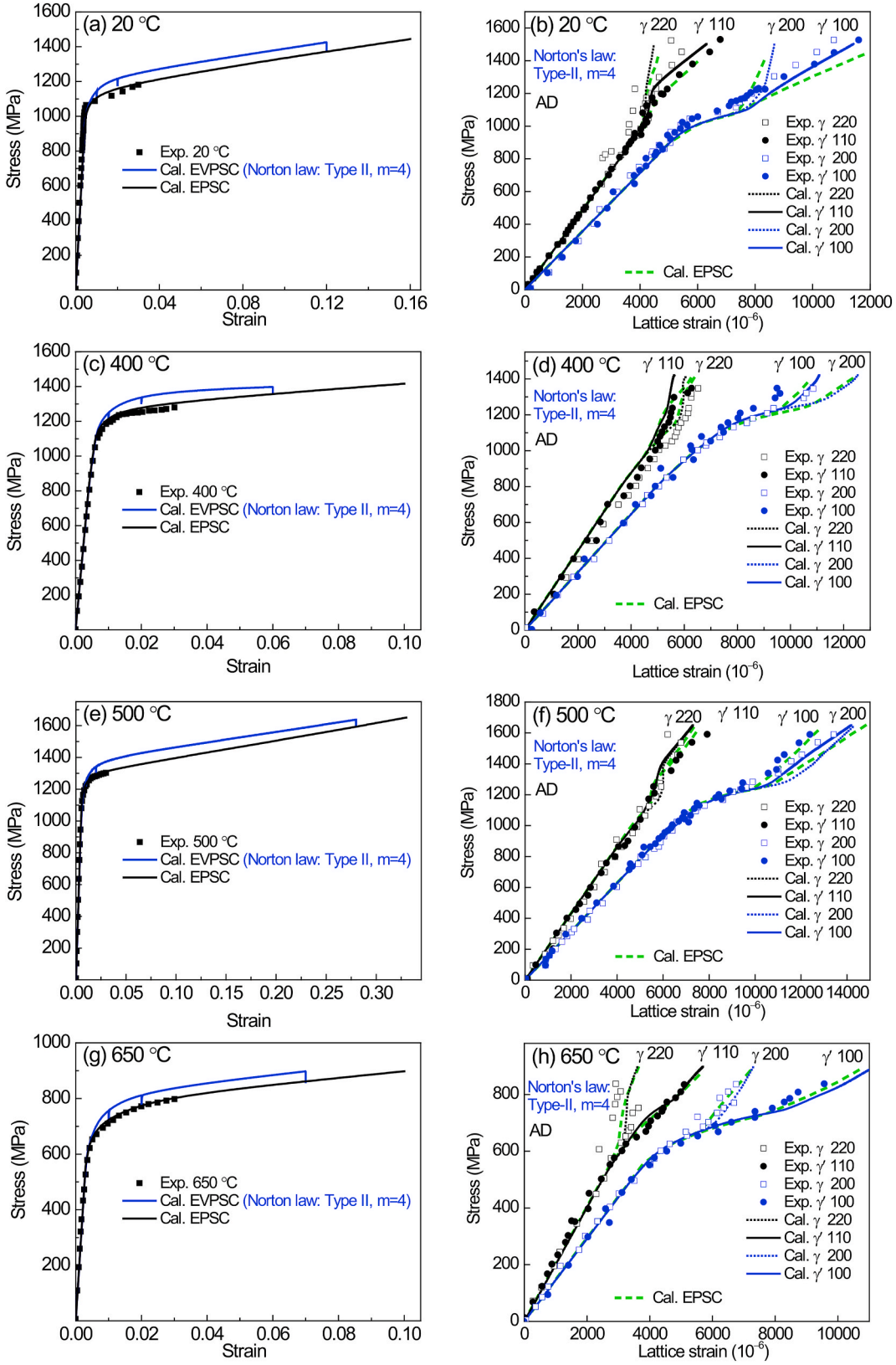

Fig. 8. Comparison of stress-strain curves and axial lattice strains measured (points, data from Ref. [10]) and simulated (lines) for Alloy 720Li utilizing Type II Norton law with fixed shear rate parameter $\dot{\gamma}_c^0 = 10^{-9}s^{-1}$ and rate-sensitive exponent $m = 4$at: (a–b) 20 °C, (c–d) 400 °C, (e–f) 500 °C, and (g–h) 650 °C. Results predicted with the 2-site EPSC model are shown as a comparison. AD stands for axial direction.

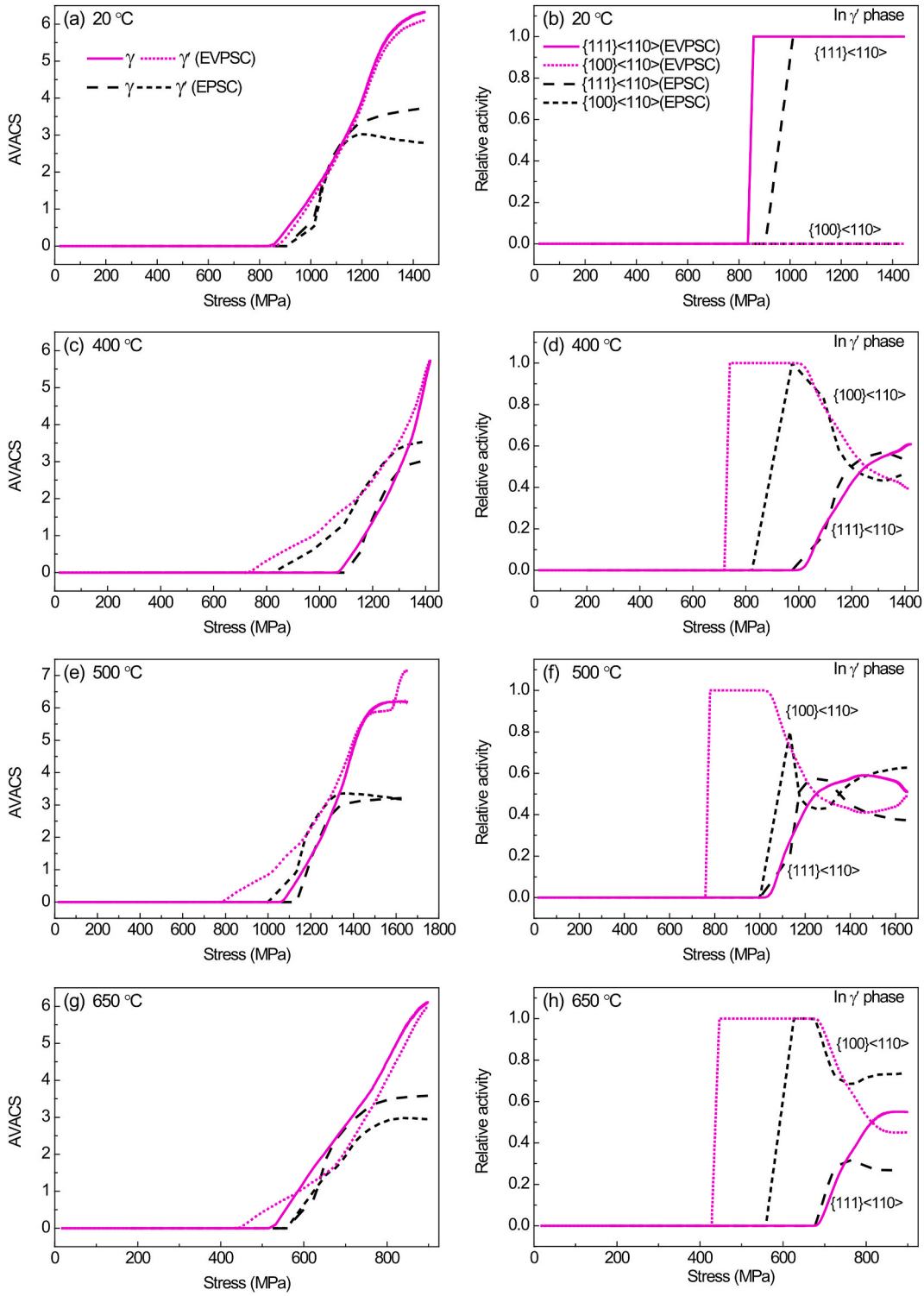

Fig. 9. Comparison of the 2-site EVPSC (Type II Norton law, $\dot{\gamma}_c^0 = 10^{-9}s^{-1}$, $m = 4$) and 2-site EPSC models on the prediction of the evolution of AVACS and relative activity of $\{111\}\langle 110\rangle$ and $\{100\}\langle 110\rangle$ slip systems in γ' phase for Alloy 720Li at:(a–b) 20 °C, (c–d) 400 °C, (e–f) 500 °C, and (g–h) 650 °C.

the two models according to the extended Voce hardening law (Eq. (7)) adjusted to best fit the experimental data is compared for the four temperatures, as shown in Fig. 12. It indicates that the initial CRSS $\tau_0$for the slip systems used in the 2-site EVPSC model is higher than that employed in the 2-site EPSC model except the $\{100\}\langle 110\rangle$slip system in γ'phase at 500 °, which is close to the peak strength temperature for Ni-based superalloys. Ni-based superalloys have the property that the yield stress at high temperatures is larger than at room temperature [44]. The result that larger $\tau_0$is used for the slip systems in the 2-site EVPSC model than that for the 2-site EPSC model is consistent with the 1-site case studied in Ref. [29] for a 316 L stainless steel where respective $\tau_0 = 84$MPa and $\tau_0 = 66$MPa are employed in the 1-site EVPSC and 1-site EPSC models, respectively. The exception observed at 500 °may connect with the reality that m depends on the temperature, as referring to the dynamic cases shown in Fig. 3 with Type I Norton law implemented in the 1-site EVPSC model, which is ignored here for the

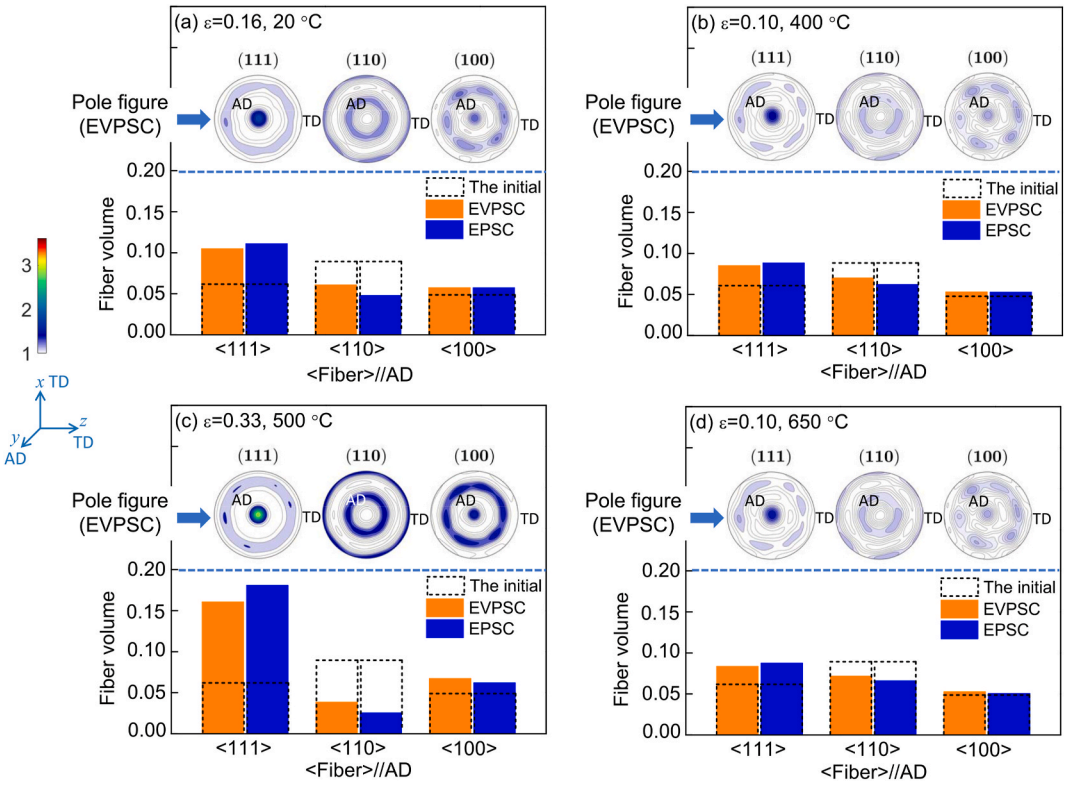

Fig. 10. Comparison of the 2-site EVPSC (Type II Norton law, $\dot{\gamma}_c^0 = 10^{-9}s^{-1}$, $m = 4$) and 2-site EPSC models on the prediction of fiber volume of ⟨111⟩, ⟨110⟩, and ⟨100⟩components parallel to the tensile axis (*i.e.* AD) for Alloy 720Li at: (a) 20 °C, (b) 400 °C, (c) 500 °C, and (d) 650 °C. The initial result is shown with dashed rectangles in each panel. Pole figures predicted by employing the 2-site EVPSC model is embedded in each panel, where AD and TD stand for axial direction and transverse direction, respectively.

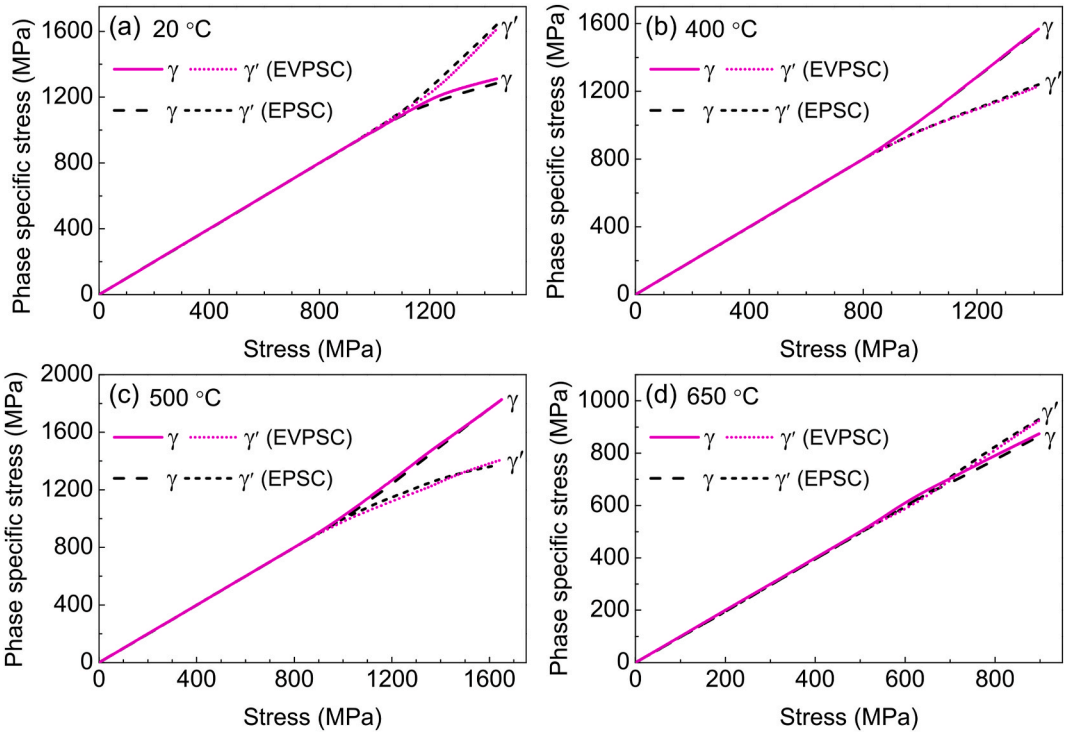

Fig. 11. Comparison of the 2-site EVPSC (Type II Norton law, $\dot{\gamma}_c^0 = 10^{-9}s^{-1}$, $m = 4$) and 2-site EPSC models on the prediction of phase specific stress of γ and γ' phases for Alloy 720Li at: (a) 20 °C, (b) 400 °C, (c) 500 °C, and (d) 650 °C.

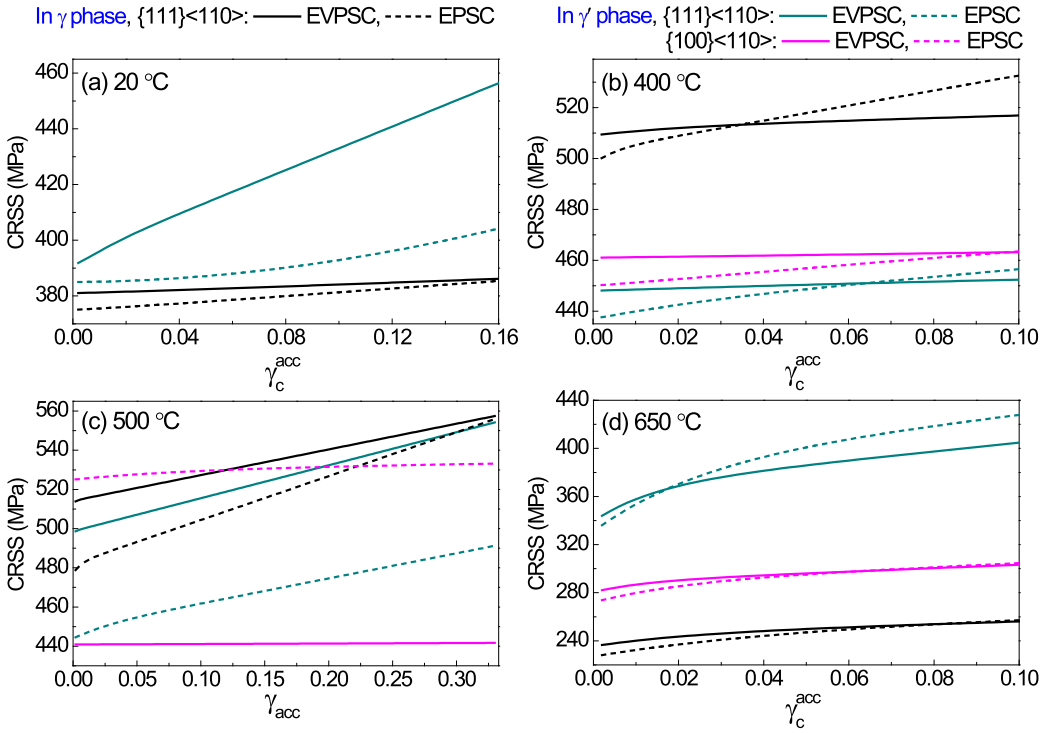

Fig. 12. Comparison of the reference hardening of individual slip systems in γ and γ' phases used in the 2-site EVPSC (Type II Norton law, $\dot{\gamma}_c^0 = 10^{-9}s^{-1}$, $m = 4$) and 2-site EPSC models according to the extended Voce hardening law (Eq. (7)) adjusted to the experimental curves of Alloy 720Li at: (a) 20 °C, (b) 400 °C, (c) 500 °C, and (d) 650 °C.

static 2-site case with Type II Norton law employed and set to be the same as $m = 4$for all the temperature cases to avoid any ambiguities caused by using different values of m while making a comparison among cases. Yet the rate-sensitive exponent m has little effect on the axial lattice strains [29], and the amount of stress relaxation does not influence the evolution of lattice strains as along as the final relaxed state is reached (comparing Fig. 7(b) with 7(d), and 7(f) and 7(h)), we do not characterize the exact value of m at each temperature.

3.4. Application of 2-site EVPSC model to transverse lattice strains of Ni-based superalloys measured by neutron diffraction under static in situ tensile tests

In this section, *in situ* neutron diffraction data of Alloy RR1000 with fine, medium, and coarse γ' microstructures at 20 °C from Ref. [1] and 750 °C from Ref. [4] is used to verify the 2-site EVPSC model on the prediction of transverse lattice strains. It should be emphasized that Type II Norton law is employed in the model with $m = 4$ and $\dot{\gamma}_c^0 = 10^{-9}\ s^{-1}$. Spherical grains are assumed for both phases at the initial state in the simulation (see microscopy pictures in Fig. 1(c) in Ref. [1] and Fig. 1 in Ref. [4]), and the interaction factor $f_{\gamma-\gamma'}$ is fixed to be 1. The same as that used in Section 3.3, 5000 grain pairs with random initial morphological and crystallographic orientation distributions are included in the model. The applied strain rate is set to be $10^{-4}s^{-1}$. Data from 10 different directions perpendicular to the loading direction is collected and averaged to present the transverse lattice strain of each reflection. The reference hardening of individual slip systems in γ and γ' phases used in the 2-site EVPSC model according to the extended Voce hardening law (Eq. (7)) is compared with that utilized in the 2-site EPSC model [11] for the selected cases. Results are plotted in Fig. 13. The initial CRSS τ_0 for the slip systems used in the 2-site EVPSC model is higher than that was used in the 2-site EPSC model for all the cases at 20 °C; however, for the cases at 750 °C, τ_0 in the 2-site EVPSC model is slightly lower than or very close to that used in the 2-site EPSC model. This may be because m should be different at high temperatures from the ambient temperature case but neglected here. Since we do not have the stress-strain curves with stress relaxations or strain creeps, the exact value of m for each case is not further calibrated here. Instead, we focus on the effect of stress relaxation, which often occurs during the traditional strain-controlled *in situ* neutron diffraction experiments, on the predicted transverse lattice strains by employing the 2-site EVPSC model.

Respective relaxation stresses of 40 MPa, 37 MPa, and 37 MPa at 20 °C and 37 MPa, 36 MPa, and 35 MPa at 750 °C at the strain of 0.01 for fine, medium, and coarse γ' microstructures are assumed. In this section, two loading modes are studied, including monotonic loading without interrupts and loading with strain holds (stress relaxation). Macroscopic stress-strain curves and lattice strains are shown in Fig. 14, where results labeled as"monotonic" and "relaxation" are respective values obtained under monotonic loading and time-averaged values during 900 s constant-strain hold in panels (c-f). For monotonic loading mode, as shown in Fig. 14(c and d), the simulated lattice strains generally fit the experimental data and approach the results predicted by the 2-site EPSC model [11] except transverse lattice strains of γ {200} and γ' {100} at the elastic-plastic transition area, where the calculated values are much larger in compression in contrast to the experiments at specific applied stresses. However, this can be greatly improved by accounting for the stress relaxation while calculating the lattice strains, as displayed in Fig. 14(e and f). Although transverse lattice strains of γ {200} and γ' {100} are improved at both temperatures, the result at 20 °C still deviates from the experimental data while that at 750 °C fits the experiments well, which is the same difficulty to deal with as it compares to the 2-site EPSC model (Fig. 13 in Ref. [11]).

3.5. Discussion on the validity of the homogenization approach for EVPSC modeling

In the proposed EVPSC models, tangent approximation of the

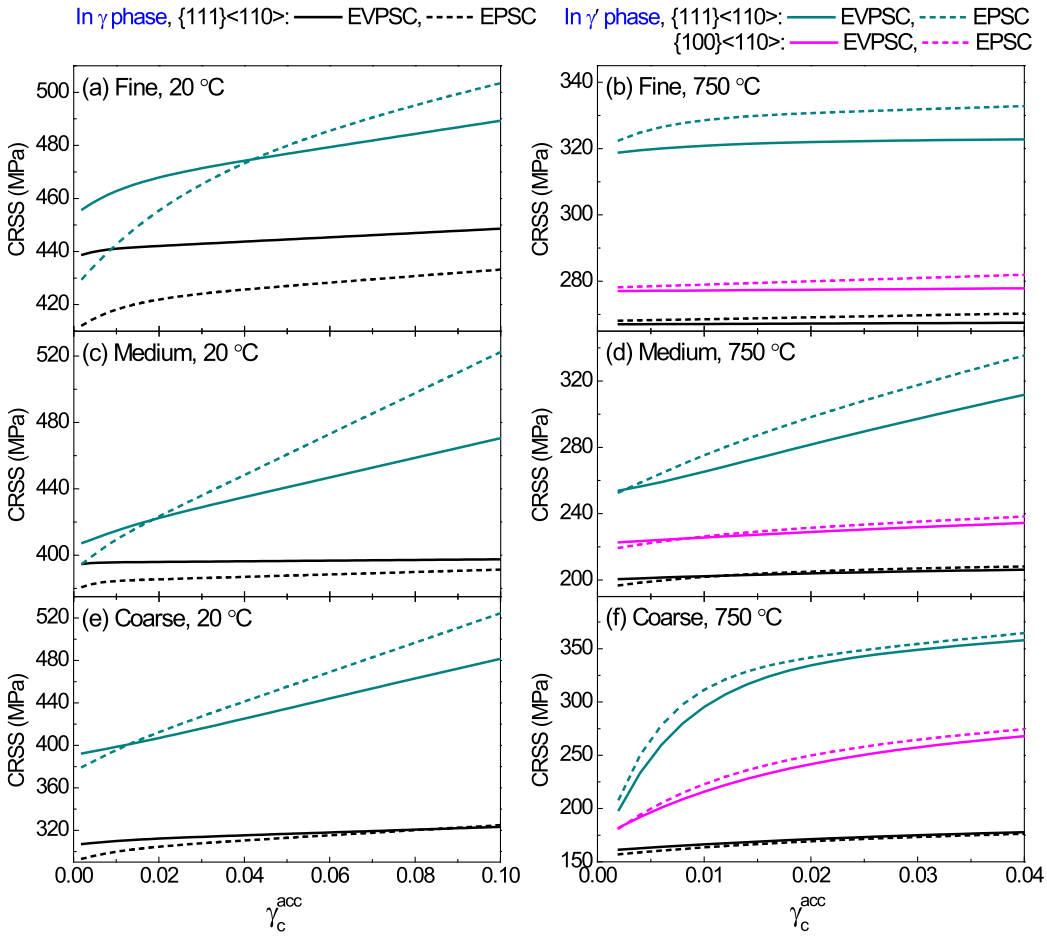

Fig. 13. Comparison of the reference hardening of individual slip systems in γ and γ′ phases used in the 2-site EVPSC and 2-site EPSC models according to the extended Voce hardening law (Eq. (7)) adjusted to the experimental curves of Alloy RR1000 with fine, medium and coarse γ′ microstructures at 20 °C and 750 °C.

constitutive law is employed for both crystals and the matrix (Eq. (12)). This approximation is valid only if the strain rate $\dot{\varepsilon}$ is not much different from the overall strain rate $\dot{\bar{\varepsilon}}$ (*i.e.* the weighted average strain rate over all the grains) [46]. Furthermore, we assume the relaxation stress rate $\dot{\bar{\sigma}}_0$ to be uniform in the matrix. It is commented that the uniform relaxation stress in the matrix leads to strong inclusion-matrix interactions [47]. Since the relaxation stress rate is associated with rate-dependent crystallographic slip and depends on the stress state (Eq. (24) and (33)), this assumption would be valid if the stress in the matrix is uniform [47]. Therefore, the heterogeneities of the material should not be too strong. We checked the normalized standard deviations of strain and stress in the grains with the 1-site EVPSC model for a single phase f.c.c. structure material deformed to a large strain of 1.0 under both dynamic compression and static tension, and with the 2-site EVPSC model for Alloy 720Li at 20 °C, 400 °C, 500 °C, and 650 °C from Refs. [10], as discussed in Section 3.3, under static tension extended to a large strain of 1.0. The normalized standard deviations of strain and stress in the grains are defined as Eq. (35):

$$\mathrm{SD}(X)_i = \frac{\sqrt{\left|\sum_{n=1}^{N} X_{n,i}^2 \omega_n - \overline{X}_i^2\right|}}{\sqrt{\sum_{i=1}^{6} \overline{X}_i^2}} \quad (i = 1,6) \tag{35}$$

where $\mathrm{SD}(X)_i$ stands for the standard deviation of the i-th component of X (strain or stress) with $i = 1,6$ in Voigt notation. $X_n$represents the strain or stress in grain number n and ω_n is the corresponding weight determined by the volume fraction. $\overline{X}_i = \sum_{n=1}^{N} X_{n,i}\omega_n$ is the i-th component of the weighted average value of the strain or stress in the grains. For the single phase material with the 1-site EVPSC model, 500 grain pairs with random initial texture is chosen. The activated slip system is assumed to be {111}⟨110⟩ type. The hardening parameters used for compression with a strain rate of 1000 s^{-1} are $\tau_0 = 43$ MPa, $\tau_1 = 29$ MPa, $\theta_0 = 60$ MPa, $\theta_1 = 1.5$ MPa, and that for tension with a strain rate of 10^{-4} s^{-1} are $\tau_0 = 81.6$MPa, $\tau_1 = 32.5$ MPa, $\theta_0 = 298$ MPa, $\theta_1 = 66.2$ MPa. Viscous parameters of Type I Norton law are $\dot{\gamma}_c^0 = 10^{-3}$ s^{-1} for both cases, and $m = 7.5$ for the dynamic compression and $m = 66$ for the static tension. Parameters employed in the 2-site EVPSC model for Alloy 720Li are the same as those used in Section 3.3 except the total grain pairs where only 500 grain pairs are chosen instead of 5000 pairs to speed up the simulation. Results are shown in Fig. 15. It reveals that the standard deviation (SD) of strain in the grains along loading direction is small for all the selected cases in this section, while that of stress severely depends on the specific plastic deformation. The SD of stress decreases as deformation progresses for the dynamic case while it increases for the static cases. The magnitude of the SD of stress is less than 0.3 within the range of strain (ε) from 0 to 1.0 for the chosen cases except for Alloy 720Li at 20 °C where the SD of stress is approaching 0.5 at $\varepsilon = 1.0$. Thus, our homogenization approach for the EVPSC model is applicable for cubic structure materials at finite strains where only slip is activated during plastic deformation, especially when $\varepsilon \leq 0.2$ (Fig. 15(b) and (d)). Its application extended to h.c.p. structure ploycrystalline materials or materials with twinning activated during plastic deformation still needs to be validated though.

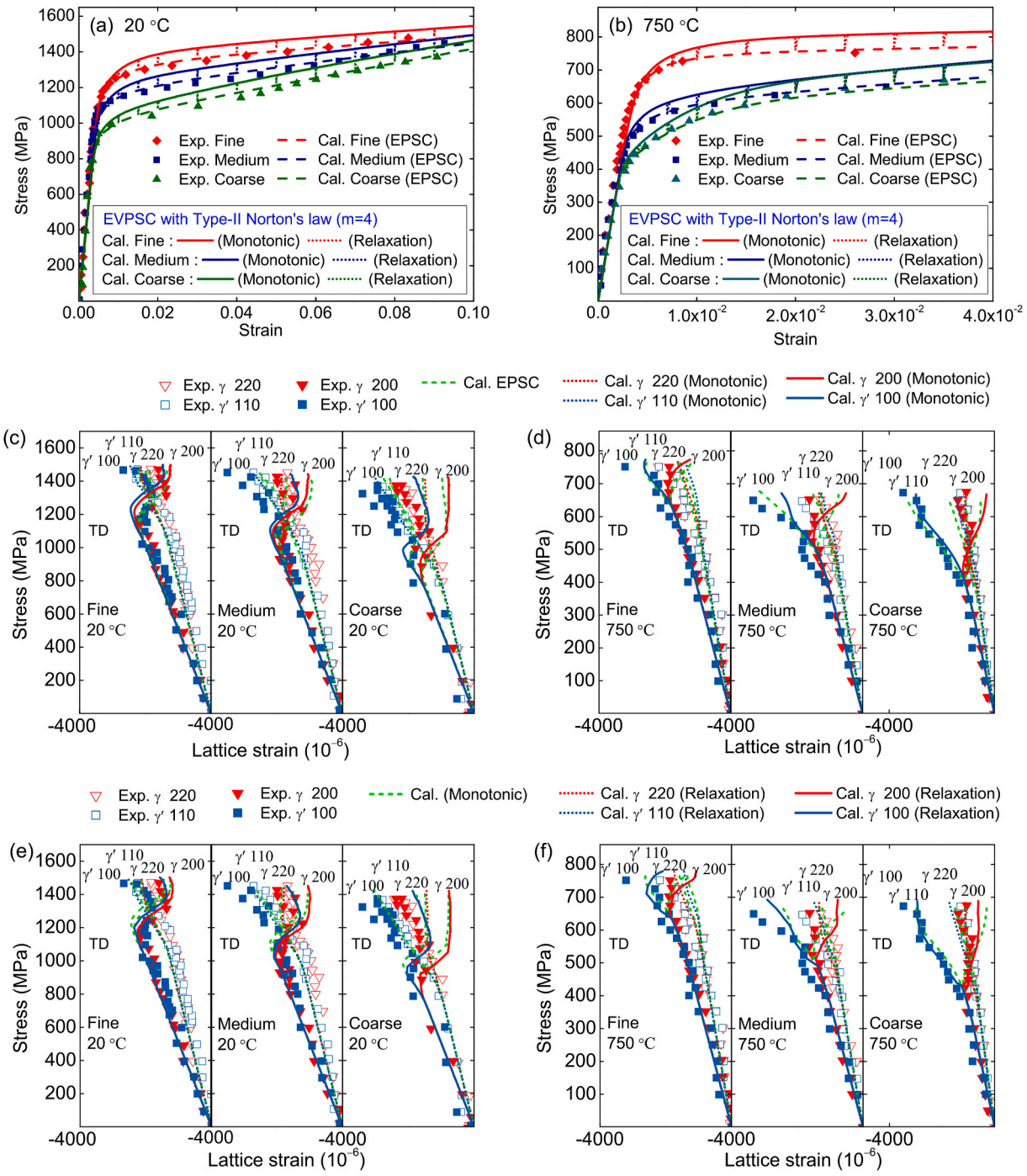

Fig. 14. Comparison of (a–b) stress-strain curves and (c–f) lattice strains measured (points, data from Ref. [1,4]) and simulated with the 2-site EVPSC model assuming different loading modes (*i.e.* monotonic loading without interrupts and loading with strain holds) for Alloy RR1000 with different γ' microstructures at 20 °C and 750 °C. Results of the 2-site EPSC model [11] are plotted as a comparison.

4. Conclusions

- 1-site and 2-site EVPSC models for finite strain applications have been developed. Type I (drag-stress type) Norton law works well for the 1-site EVPSC model while Type II (threshold stress type) Norton law should be used in the 2-site EVPSC model to assure that the viscoplastic inter-granular interaction is realistic. The advantage of the proposed EVPSC models in this work is that all mathematical conveniences of the linear Eshelby solution from the 1-site and 2-site EPSC models are retained.
- The 1-site EVPSC model has been verified firstly by fitting the dynamic stress-strain curves at different strain rates and temperatures for a 316 L stainless steel and a Fe-based high temperature alloy. It has also been tested on the prediction of static mechanical response during *in situ* neutron diffraction. Applied stress versus lattice strain curves for a 316 L stainless steel have been well fitted with an exception that transverse lattice strains of {200} have relatively larger deviations from the experimental comparing to other crystalline planes. Nevertheless, the predictions of the transverse {200} behavior was better predicted by the EVPSC model compared to the EPSC model.

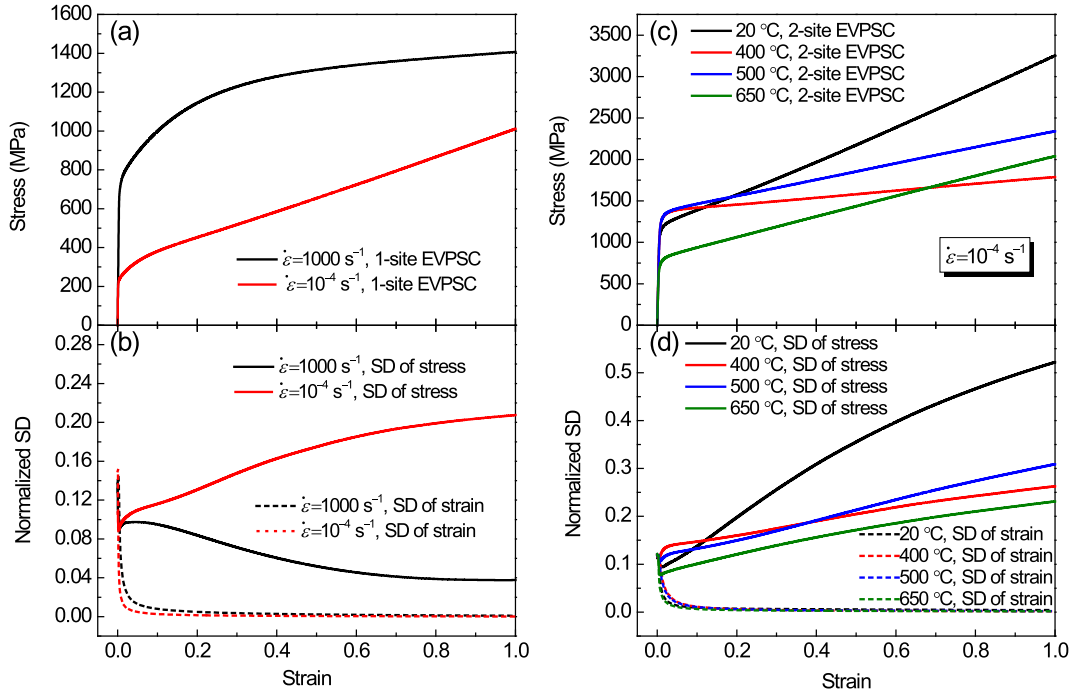

Fig. 15. Dynamic compression and static tension deformed to a large strain of 1.0 for a single phase f.c.c. structure material with the 1-site EVPSC model, and static tension extended to a large strain of 1.0 for Alloy 720Li at various temperatures discussed in Section 3.3 from Ref. [10] with the 2-site EVPSC model: (a) and (c) stress-strain curves, (b) and (d) corresponding normalized standard deviations of strain and stress in the grains along loading direction. SD in Panels (b) and (d) stands for standard deviation.

- The 2-site EVPSC model is firstly applied to predict axial lattice strains of Alloy 720Li with intermixed γ' precipitates at ambient and elevated temperatures. The anomalous behavior of Ni-based superalloys below the peak strength temperature around 500 °has been well captured. Although there are obvious deviations from the experimental data in the prediction of axial lattice strains at relatively large strains at 500 °, the overall evolution and magnitude of the simulated results are acceptable. It has also been compared to the 2-site EPSC model in the prediction of AVACS, relative activity of $\{111\}\langle 110\rangle$ and $\{100\}\langle 110\rangle$ slip systems in γ' phase, deformed texture, and phase specific stress of γ and γ' phases. Similar conclusions can be drawn from the two models with some small differences.
- The 2-site EVPSC model is also applied to predict transverse lattice strains of Alloy RR1000 with fine, medium, and coarse γ' microstructures at 20 °C and 750 °C. Simulated lattice strains of loading with strain holds are more approaching to the experimental data than those of monotonic loading, which indicates that the effect of stress relaxation on the measured and/or simulated lattice strains cannot be neglected. The model generally fits the experimental data well except for transverse lattice strains of γ {200} and γ' {100} at 20 °C, which is the same difficulty to deal with as it compares to the 2-site EPSC model proposed previously by the authors.
- A validation of the homogenization approach for the EVPSC models has been done by studying the normalized standard deviations of strain and stress in the grains under both dynamic compression and static tension up to the strain 1.0. The results indicate that the heterogeneities of the selected materials at finite strains are not strong, especially when $\varepsilon \leq 0.2$. It is confirmed that the proposed EVPSC models are applicable for cubic structure materials with finite deformations where only slip is activated during plastic deformation. Their applicability to h.c.p. structure polycrystalline materials or materials with twinning activated during plastic deformation still needs to be validated and it is underway.

CRediT authorship contribution statement

Hongjia Li: Conceptualization, Software, Validation, Writing - original draft. **Fredrik Larsson:** Conceptualization, Methodology, Supervision. **Magnus Hörnqvist Colliander:** Conceptualization, Project administration, Funding acquisition. **Magnus Ekh:** Conceptualization, Methodology, Writing - review & editing, Supervision, Project administration, Funding acquisition.

Declaration of competing interest

The authors declare that they have no known competing financial interests or personal relationships that could have appeared to influence the work reported in this paper.

Acknowledgements

The work was funded by the Chalmers University of Technology Foundation through the project "Center for advanced neutron and x-ray scattering techniques" and Area of Advance Materials Science at Chalmers University of Technology. The work of Hongjia Li was also supported by the Foundation of President of CAEP (Grant YZJJLX2019004) and the Key Laboratory Foundation for Neutron Physics of CAEP (Grant 2019AB01). The simulations were performed on resources provided by Chalmers Center for Computational Science and Engineering (C3SE).

Appendix A. Details of finite strain approach for EVPSC modeling

Appendix A.1 Accounting for texture evolution at arbitrary strains

Rotations of the sample, ellipsoid, and crystal lattice are taken into account [48].

(1) Applied macroscopic rotation rate:

$$\dot{\boldsymbol{\Omega}} = \frac{1}{2}\left(\boldsymbol{l} - \boldsymbol{l}^{\mathrm{T}}\right) \tag{A.1}$$

where $\boldsymbol{l}$is the macroscopic velocity gradient.

(2) Local rotation rate:

$$\dot{\boldsymbol{\omega}}_c = \dot{\boldsymbol{\Omega}} + \dot{\tilde{\boldsymbol{\omega}}}_c \tag{A.2}$$

where $\dot{\tilde{\boldsymbol{\omega}}}_c$is the deviation from the macroscopic rotation rate, of which the expressions are given in terms of Eshelby tensors in Ref. [48] for the 1-site SC models and [11,20] for the 2-site SC models.

(3) Crystal lattice rotation rate:

$$\dot{\boldsymbol{\omega}}_c^{\mathrm{lat}} = \dot{\boldsymbol{\omega}}_c - \dot{\boldsymbol{\omega}}_c^{\mathrm{pl}} \tag{A.3}$$

with the plastic rotation rate $\dot{\boldsymbol{\omega}}_c^{\mathrm{pl}}$taking the form:

$$\dot{\boldsymbol{\omega}}_c^{\mathrm{pl}} = \sum_{\alpha} \boldsymbol{q}_c^{\alpha} \dot{\gamma}_c^{\alpha} \tag{A.4}$$

where $\boldsymbol{q}_c^{\alpha} = \mathrm{skw}\left(\boldsymbol{b}_c^{\alpha} \otimes \boldsymbol{n}_c^{\alpha}\right)$is the skew-symmetric Schmid tensor, and $\dot{\gamma}_c^{\alpha}$is the shear rate on the α-th slip system.

For the 2-site model, further considerations must be taken in order to accurately describe the strong correlation in both morphology and crystallographic orientation between the ellipsoidal inclusions within each pair. In order to address the former, weighted average local rotation rate is used [11]:

$$\dot{\boldsymbol{\omega}}_{\mathrm{ave}} = w_1\, \dot{\boldsymbol{\omega}}_1 + w_2\, \dot{\boldsymbol{\omega}}_2 \tag{A.5}$$

where $w_1$and $w_2$are the volume fractions of each phase. As a result, the crystal lattice rotation rate calculated via Eq.(A.3) is changed into the following form:

$$\dot{\boldsymbol{\omega}}_c^{\mathrm{lat}} = \dot{\boldsymbol{\omega}}_{\mathrm{ave}} - \dot{\boldsymbol{\omega}}_c^{\mathrm{pl}} \tag{A.6}$$

In order to account for the latter, crystal lattice co-rotation rate is used in the 2-site EVPSC model [11]:

$$\dot{\boldsymbol{\omega}}_{\mathrm{corot}}^{\mathrm{lat}} = \frac{1}{2}\left(\dot{\boldsymbol{\omega}}_1^{\mathrm{lat}} + \dot{\boldsymbol{\omega}}_2^{\mathrm{lat}}\right) \tag{A.7}$$

Appendix A.2 An approximate finite strain algorithm

Similar to Neil et al. [39], the Jaumann rate of the Cauchy stress $\hat{\boldsymbol{\sigma}}_c$is introduced to account for crystal lattice rotation (Eq.(A.3)) or co-rotation (Eq. (A.7)) for the 1-site and 2-site EVPSC models, respectively. The constitutive rules for both grain level (Eq. (12a)) and macroscopic scale (Eq. (12b)) are rewritten:

$$\hat{\boldsymbol{\sigma}}_{\mathrm{c}} = \mathbf{L}_{\mathrm{c}} : d_{\mathrm{c}} + \dot{\boldsymbol{\sigma}}_{\mathrm{c}}^{0} \tag{A.8a}$$

$$\hat{\boldsymbol{\sigma}} = \overline{\mathbf{L}} : \boldsymbol{d} + \dot{\bar{\boldsymbol{\sigma}}}_0 \tag{A.8b}$$

In this approximate approach, the SC equations in Section 2.2 are modified with replacing $\dot{\bar{\boldsymbol{\sigma}}}$, $\dot{\boldsymbol{\sigma}}_{\mathrm{c}}$, $\dot{\bar{\varepsilon}}$, and $\dot{\varepsilon}_{\mathrm{c}}$by $\hat{\boldsymbol{\sigma}}$, $\hat{\boldsymbol{\sigma}}_{\mathrm{c}}$, $\boldsymbol{d}$, and $\boldsymbol{d}_{\mathrm{c}}$, respectively. After solving the ellipsoidal inclusion equilibrium equation and reaching convergence, all Cauchy stress rates are updated to the reference coordinate system using the definition of the Jaumann derivative as follows:

$$\dot{\boldsymbol{\sigma}}_{\mathrm{c}} = \hat{\boldsymbol{\sigma}}_{\mathrm{c}} + \dot{\boldsymbol{\omega}}_{\mathrm{c}}^{\mathrm{lat}}\, \boldsymbol{\sigma}_{\mathrm{c}} - \boldsymbol{\sigma}_{\mathrm{c}}\, \dot{\boldsymbol{\omega}}_{\mathrm{c}}^{\mathrm{lat}} \tag{A.9a}$$

$$\dot{\bar{\boldsymbol{\sigma}}} = \hat{\boldsymbol{\sigma}} + \dot{\boldsymbol{\Omega}}\, \bar{\boldsymbol{\sigma}} - \bar{\boldsymbol{\sigma}}\, \dot{\boldsymbol{\Omega}} \tag{A.9b}$$

where $\dot{\boldsymbol{\omega}}_{\mathrm{c}}^{\mathrm{lat}}$should be computed with Eqs.(A.3) and (A.7) for the 1-site and 2-site EVPSC models, respectively.

Appendix A.3 Schemes to update the material state

The following updates should be introduced after reaching self-consistency for the finite strain SC approach [11,12,39]:

(1) Deformation and reorientation of ellipsoids: In the 1-site model, velocity gradient of a crystal ($\boldsymbol{l}_c$) is used to update the shape of the ellipsoid. In the 2-site model, we use the weighted average velocity gradient of the two ellipsoids within a pair ($\boldsymbol{l}_{\text{ave}} = w_1\,\boldsymbol{l}_1 + w_2\,\boldsymbol{l}_2$) to update the shape of each ellipsoid in order to allow each ellipsoid to deform individually with the constraint from its partner. The deformation gradient of each ellipsoid at the i-th time step is defined as:

$$\boldsymbol{F}_c^{i+1} = \left(\boldsymbol{I} + \boldsymbol{l}_{\text{c}}^{i}\,\Delta t\right)\cdot\boldsymbol{F}_c^{i} \tag{A.10a}$$

$$\boldsymbol{F}_c^{i+1} = \left(\boldsymbol{I} + \boldsymbol{l}_{\text{ave}}^{i}\,\Delta t\right)\cdot\boldsymbol{F}_c^{i} \tag{A.10b}$$

where Eqs.(A.10a) and (A.10b) are for 1-site and 2-site cases, respectively. It should be noted that $\boldsymbol{l}_{\text{c}} = \boldsymbol{d}_{\text{c}} + \dot{\boldsymbol{\omega}}_{\text{c}}$and $\boldsymbol{l}_{\text{ave}} = \boldsymbol{d}_{\text{ave}} + \dot{\boldsymbol{\omega}}_{\text{ave}}$with $\boldsymbol{d}_{\text{ave}} = w_1\,\boldsymbol{d}_1 + w_2\,\boldsymbol{d}_2$, and the contributions of $\dot{\boldsymbol{\omega}}_{\text{c}}$and $\dot{\boldsymbol{\omega}}_{\text{ave}}$are taken into account in a separate step (see Item (2) below). The updated shape and orientation of the ellipsoid is given by the square root of eigenvalues and eigenvectors of $\boldsymbol{F}\cdot\boldsymbol{F}^{\text{T}}$.

(2) Rotations of ellipsoid and crystal lattice: Rodrigues' rotation formula is used to update the morphological orientation with $\dot{\boldsymbol{\omega}}_{\text{c}}$for the 1-site case (Eq.(A.2)) and $\dot{\boldsymbol{\omega}}_{\text{ave}}$for the 2-site case (Eq.(A.5)), and the crystallographic orientation with $\dot{\boldsymbol{\omega}}_{c}^{\text{lat}}$for the 1-site case (Eq.(A.3)) and $\dot{\boldsymbol{\omega}}_{\text{corot}}^{\text{lat}}$(Eq.(A.7)) for the 2-site case.

(3) More updates for the 2-site EVPSC model [11]: The relative position of the two ellipsoids within each pair is rotated with $\dot{\boldsymbol{\omega}}_{\text{ave}}$(Eq.(A.5)) in order to follow the rotation of the local coordinate system. The distance between the two ellipsoids is also updated by adding up the average length of the three principal axes of ellipsoid # 1 and that of ellipsoid # 2.

References

[1] B.M.B. Grant, E.M. Francis, J.Q. da Fonseca, M.R. Daymond, M. Preuss, Deformation behaviour of an advanced nickel-based superalloy studied by neutron diffraction and electron microscopy, Acta Mater. 60 (19) (2012) 6829–6841, https://doi.org/10.1016/j.actamat.2012.09.005.

[2] S.R. Agnew, R.P. Mulay, F.J. Polesak, C.A. Calhoun, J.J. Bhattacharyya, B. Clausen, In situ neutron diffraction and polycrystal plasticity modeling of a mg-y–nd–zr alloy: effects of precipitation on individual deformation mechanisms, Acta Mater. 61 (10) (2013) 3769–3780, https://doi.org/10.1016/j.actamat.2013.03.010.

[3] D.W. Brown, B. Clausen, T.A. Sisneros, L. Balogh, I.J. Beyerlein, In situ neutron diffraction measurements during annealing of deformed beryllium with differing initial textures, Metall. Mater. Trans. 44 (2013) 5665–5675, https://doi.org/10.1007/s11661-013-1932-3.

[4] E.M. Francis, B.M.B. Grant, J.Q. da Fonseca, P.J. Phillips, M.J. Mills, M. R. Daymond, M. Preuss, High-temperature deformation mechanisms in a polycrystalline nickel-base superalloy studied by neutron diffraction and electron microscopy, Acta Mater. 74 (2014) 18–29, https://doi.org/10.1016/j.actamat.2014.04.028.

[5] V. Hounkpati, S. Fréour, D. Gloaguen, V. Legrand, J. Kelleher, W. Kockelmann, S. Kabra, In situ neutron measurements and modelling of the intergranular strains in the near-β titanium alloy ti-β21s, Acta Mater. 109 (2016) 341–352, https://doi.org/10.1016/j.actamat.2016.02.065.

[6] M. Yang, F. Yuan, Q. Xie, Y. Wang, E. Ma, X. Wu, Strain hardening in fe–16mn–10al–0.86c–5ni high specific strength steel, Acta Mater. 109 (2016) 213–222, https://doi.org/10.1016/j.actamat.2016.02.044.

[7] C.A. Calhoun, E. Garlea, T.A. Sisneros, S.R. Agnew, In-situ neutron diffraction characterization of temperature dependence deformation in α-uranium, J. Nucl. Mater. 502 (2018) 60–67, https://doi.org/10.1016/j.jnucmat.2018.01.036.

[8] M. Yang, R. Li, P. Jiang, F. Yuan, Y. Wang, Y. Zhu, X. Wu, Residual stress provides significant strengthening and ductility in gradient structured materials, Materials Research Letters 7 (11) (2019) 433–438, https://doi.org/10.1080/21663831.2019.1635537.

[9] N.R. Jaladurgam, H. Li, J. Kelleher, C. Persson, A. Ateuwer, M.H. Colliander, Microstructure-dependent deformation behaviour of a low γ' volume fraction ni-base superalloy studied by in-situ neutron diffraction, Acta Mater. 183 (2020) 182–195, https://doi.org/10.1016/j.actamat.2019.11.003.

[10] M.R. Daymond, M. Preuss, B. Clausen, Evidence of variation in slip mode in a polycrystalline nickel-base superalloy with change in temperature from neutron diffraction strain measurements, Acta Mater. 55 (9) (2007) 3089–3102, https://doi.org/10.1016/j.actamat.2007.01.013.

[11] H. Li, M. Ekh, M. H, Accounting for lattice coherency in a two-phase elastic-plastic self-consistent model for nickel-based superalloys, Int. J. Plast. 110 (2018) 248–271.

[12] P.A. Turner, C.N. Tomé, A study of residual stresses in zircaloy-2 with rod texture, Acta Metall. Mater. 42 (12) (1994) 4143–4153, https://doi.org/10.1016/0956-7151(94)90191-0.

[13] R.A. Lebensohn, C.N. Tomé, A self-consistent anisotropic approach for the simulation of plastic deformation and texture development of polycrystals: application to zirconium alloys, Acta Metall. Mater. 41 (9) (1993) 2611–2624, https://doi.org/10.1016/0956-7151(93)90130-K.

[14] R. Hill, Continuum micro-mechanics of elastoplastic polycrystals, J. Mech. Phys. Solid. 13 (2) (1965) 89–101, https://doi.org/10.1016/0022-5096(65)90023-2.

[15] J.W. Hutchinson, Elastic-plastic behaviour of polycrystalline metals and composites, Proc. Roy. Soc. Lond.: Mathematical, Physical and Engineering Sciences 319 (1537) (1970) 247–272, https://doi.org/10.1098/rspa.1970.0177.

[16] J.D. Eshelby, The determination of the elastic field of an ellipsoidal inclusion, and related problems, Proc. Roy. Soc. Lond.: Mathematical, Physical and Engineering Sciences 241 (1226) (1957) 376–396.

[17] G.I. Taylor, Plastic strain in metals, J. Inst. Met. 62 (1938) 307–324.

[18] S. Ankem, H. Margolin, The role of elastic interaction stresses on the onset of plastic flow for oriented two ductile phase structures, Metallurgical Transactions A 11A (6) (1980) 963–972, https://doi.org/10.1007/BF02654710.

[19] C.T. Sims, N.S. Stoloff, W.C. Hagel, Superalloys II: High-Temperature Materials for Aerospace and Industrial Power, John Wiley & Sons, New York, 1987.

[20] R.A. Lebensohn, G.R. Canova, A self-consistent approach for modelling texture development of two-phase polycrystals: application to titanium alloys, Acta Mater. 45 (9) (1997) 3687–3694, https://doi.org/10.1016/S1359-6454(97)00067-0.

[21] N.-N. S, O. M, H. Rodney, Rate-dependent, finite elasto-plastic deformation of polycrystals, Proc. Roy. Soc. Lond. 407 (1986) 343–375, https://doi.org/10.1098/rspa.1986.0101.

[22] A. Paquin, S. Berbenni, V. Favier, X. Lemoine, M. Berveiller, Micromechanical modeling of the elastic-viscoplastic behavior of polycrystalline steels, Int. J. Plast. 17 (9) (2001) 1267–1302, https://doi.org/10.1016/S0749-6419(00)00047-4.

[23] S. Mercier, A. Molinari, Homogenization of elastic-viscoplastic heterogeneous materials: self-consistent and mori-tanaka schemes, Int. J. Plast. 25 (6) (2009) 1024–1048, https://doi.org/10.1016/j.ijplas.2008.08.006.

[24] H. Wang, P. Wu, C.N. Tomé, Y. Huang, A finite strain elastic-viscoplastic self-consistent model for polycrystalline materials, J. Mech. Phys. Solid. 58 (4) (2010) 594–612, https://doi.org/10.1016/j.jmps.2010.01.004.

[25] H. Wang, P. Wu, S. Kurukuri, M.J. Worswick, Y. Peng, D. Tang, D. Li, Strain rate sensitivities of deformation mechanisms in magnesium alloys, Int. J. Plast. 107 (2018) 207–222, https://doi.org/10.1016/j.ijplas.2018.04.005.

[26] Y. Jeong, C.N. Tomé, Extension of the vpsc model to account for elasto-visco-plastic behavior using a perturbed viscoplastic approach, Model. Simulat. Mater. Sci. Eng. 27 (8) (2019), 085013, https://doi.org/10.1088/1361-651X/ab4b66.

[27] A. Molinari, F.E. Houdaigui, L. Tóth, Validation of the tangent formulation for the solution of the non-linear eshelby inclusion problem, Int. J. Plast. 20 (2) (2004) 291–307, https://doi.org/10.1016/S0749-6419(03)00038-X.

[28] S. Mercier, N. Jacques, A. Molinari, Validation of an interaction law for the eshelby inclusion problem in elasto-viscoplasticity, Int. J. Solid Struct. 42 (7) (2005) 1923–1941, https://doi.org/10.1016/j.ijsolstr.2004.08.016.

[29] H. Wang, B. Clausen, C.N. Tomé, P. Wu, Studying the effect of stress relaxation and creep on lattice strain evolution of stainless steel under tension, Acta Mater. 61 (4) (2013) 1179–1188, https://doi.org/10.1016/j.actamat.2012.10.027.

[30] X. Guo, P.D. Wu, H. Wang, X.B. Mao, Study of lattice strain evolution in stainless steel under tension: the role of self-consistent plasticity model, Steel Res. Int. 86 (8) (2015) 894–901, https://doi.org/10.1002/srin.201400570.

[31] H. Wang, P. Wu, C.N. Tomé, J. Wang, Study of lattice strains in magnesium alloy az31 based on a large strain elastic-viscoplastic self-consistent polycrystal model, Int. J. Solid Struct. 49 (15) (2012) 2155–2167, https://doi.org/10.1016/j.ijsolstr.2012.04.026.

[32] S.Y. Lee, H. Wang, M.A. Gharghouri, G. Nayyeri, W. Woo, E. Shin, P. Wu, W. J. Poole, W. Wu, K. An, Deformation behavior of solid-solution-strengthened mg-9 wt.% al alloy: in situ neutron diffraction and elastic-viscoplastic self-consistent modeling, Acta Mater. 73 (2014) 139–148, https://doi.org/10.1016/j.actamat.2014.03.038.
[33] H. Qiao, P. Wu, H. Wang, M.A. Gharghouri, M.R. Daymond, Evaluation of elastic-viscoplastic self-consistent polycrystal plasticity models for zirconium alloys, Int. J. Solid Struct. 71 (2015) 308–322, https://doi.org/10.1016/j.ijsolstr.2015.07.004.
[34] K. Hutter, H. Baaser, Deformation and Failure in Metallic Materials, Springer-Verlag, Berlin Heidelberg, 2003.
[35] N.S. Ottosen, M. Ristinmaa, The Mechanics of Constitutive Modeling, Elsevier Science & Technology, 2005.
[36] C.N. Tomé, P.J. Maudlin, R.A. Lebensohn, G.C. Kaschner, Mechanical response of zirconium-i. derivation of a polycrystal constitutive law and finite element analysis, Acta Mater. 49 (15) (2001) 3085–3096, https://doi.org/10.1016/S1359-6454(01)00190-2.
[37] R.A. Lebensohn, P.A. Turner, J.W. Signorelli, G.R. Canova, C.N. Tomé, Calculation of intergranular stresses based on a large-strain viscoplastic self-consistent polycrystal model, Model. Simulat. Mater. Sci. Eng. 6 (1998) 447–465, https://doi.org/10.1088/0965-0393/6/4/011.
[38] M. Berveiller, O. Fassi-Fehri, A. Hihi, The problem of two plastic and heterogeneous inclusions in an anisotropic medium, Int. J. Eng. Sci. 25 (6) (1987) 691–709, https://doi.org/10.1016/0020-7225(87)90058-9.
[39] C.J. Neil, J.A. Wollmershauser, B. Clausen, C.N. Tomé, S.R. Agnew, Modeling lattice strain evolution at finite strains and experimental verification for copper and stainless steel using in situ neutron diffraction, Int. J. Plast. 26 (12) (2010) 1772–1791, https://doi.org/10.1016/j.ijplas.2010.03.005.
[40] W.-S. Lee, T.-H. Chen, C.-F. Lin, W.-Z. Luo, Dynamic mechanical response of biomedical 316l stainless steel as function of strain rate and temperature, Bioinorgan. Chem. Appl. 2011 (2011) 1–13, https://doi.org/10.1155/2011/173782.
[41] X. Su, G. Wang, J. Li, Y. Rong, Dynamic mechanical response and a constitutive model of fe-based high temperature alloy at high temperatures and strain rates, Springer Plus 5 (2016) 504–517, https://doi.org/10.1186/s40064-016-2169-6.
[42] P. Larour, A. Bäumer, K. Dahmen, W. Bleck, Influence of strain rate, temperature, plastic strain, and microstructure on the strain rate sensitivity of automotive sheet steels, Steel Res. Int. 84 (5) (2013) 426–442, https://doi.org/10.1002/srin.201200099.
[43] V. Talyan, R.H. Wagoner, J.K. Lee, Formability of stainless steel, Metall. Mater. Trans. 29A (1998) 2161–2172, https://doi.org/10.1007/s11661-998-0041-1.
[44] P.H. Thornton, R.G. Davies, T.L. Johnston, The temperature dependence of the flow stress of the γ' phase based upon ni3al, Metallurgical Transactions 1 (1) (1970) 207–218, https://doi.org/10.1007/BF02819263.
[45] R. Hielscher, H. Schaeben, A novel pole figure inversion method: specification of the *MTEX* algorithm, J. Appl. Crystallogr. 41 (6) (2008) 1024–1037, https://doi.org/10.1107/S0021889808030112.
[46] A. Molinari, G. Canova, S. Ahzi, A self consistent approach of the large deformation polycrystal viscoplasticity, Acta Metall. 35 (12) (1987) 2983–2994, https://doi.org/10.1016/0001-6160(87)90297-5.
[47] R. Kouddane, A. Molinari, G.R. Canova, Self-consistent modelling of heterogeneous viscoelastic and elastoviscoplastic materials, in: Teodosiu, Raphanel, Sidoroff (Eds.), Large Plastic Deformations, Fundamentals and Applications to Metal Forming. Balkerma, Rotterdam, the Neterlands, 1993.
[48] C.N. Tomé, R.A. Lebensohn, C.T. Necker, Mechanical anisotropy and grain interaction in recrystallized aluminum, Metall. Mater. Trans. 33A (8) (2002) 2635–2648, https://doi.org/10.1007/s11661-002-0385-x.